SMOS brightness temperature forward modelling, bias correction and long term monitoring at ECMWF

Patricia de Rosnay[a,*], Joaquín Muñoz Sabater[a], Clément Albergel[a,1], Lars Isaksen[a], Matthias Drusch[b], Jean-Pierre Wigneron[c]

[a] *European Centre for Medium-Range Weather Forecasts (ECMWF), Shinfield Park, RG2 9AX, Reading, UK*
[b] *European Space Agency, ESTEC, Noordwijk, the Netherlands*
[c] *Interactions Sol Plante Atmosphère (ISPA), Unité Mixte de Recherche 1391, Institut National de la Recherche Agronomique (INRA), CS 20032, 33882 Villenave d'Ornon CEDEX, France*

Abstract

This paper presents the European Centre for Medium-Range Weather Forecasts (ECMWF) radiative transfer modelling activities conducted to use Soil Moisture and Ocean Salinity (SMOS) brightness temperature observations for Numerical Weather Forecast (NWP) applications. The Community Microwave Emission Modelling Platform (CMEM) is used as the ECMWF SMOS forward operator to simulate L-band brightness temperatures (TBs). In a first part, simulated brightness temperature are compared to the observed SMOS near real time reprocessed brightness temperature product for 2010-2011 for several configurations of CMEM using different set of parameterisations. We show that simulated brightness temperatures are more sensitive to the choice of vegetation opacity and soil roughness models than to the dielectric model. Best configurations of CMEM are shown to be those using the so-called Wigneron vegetation opacity model with the simple empirical Wigneron soil roughness model. The Wang and Schmugge and the Mironov soil dielectric models perform similarly and lead to better agreement with SMOS observations than the Dobson dielectric model. Based on this intercomparison the configuration of CMEM retained for ECMWF SMOS forward modelling activities is the one based the Wang and Schmugge dielectric model, the Wigneron simple roughness model and the Wigneron vegetation model. In a second part, this paper presents the SMOS brightness temperature bias correction developed and used at ECMWF. It is a monthly Cumulative Distribution Function bias correction based on SMOS and ECMWF re-analysis-based brightness temperatures for the period from 1 January 2010 to 31 December 2013. Results show that it efficiently corrects for systematic differences between observations and model, with global root mean square differences (RMSD) and global mean bias for 2010-2013 for 30° 40°, 50° incidence angles decreasing from 16.7 K and -2.1 K before bias correction to 7.91K and 0.0016 K after bias correction, respectively. The monthly approach allows to correct for seasonal cycles systematic differences, with correlation values improved from 0.56 before bias correction and 0.62 after bias correction. Residual differences remaining after bias correction correspond to random differences between the model and observations which provide relevant information for monitoring and data assimilation purposes. Finally, in a third part long term monitoring of SMOS brightness temperature monitoring is presented covering a 7-year period 2010-2016 at both polarisations, at 40 degrees incidence angle. RMSD, correlation and anomaly correlation statistics show that SMOS and ECMWF reanalysis-based brightness temperature

agreement steadily improves between 2010 and 2016, indicating improvement of SMOS products quality through the SMOS lifetime.
Keywords: SMOS, L-Band, forward modelling, CMEM, bias correction, reanalysis, monitoring

1. Introduction

Soil moisture is a key variable of the Earth System. It has a large influence on the exchange processes between land surfaces and the atmosphere and it largely controls the water and energy budgets (Taylor et al., 2012; Koster et al., 2004; Trenberth et al., 2007). Initial state of soil moisture influences weather prediction at at medium range (de Rosnay et al., 2013; Drusch, 2007) and at seasonal range (Koster et al., 2011) . It is also of crucial importance for agricultural drought monitoring (Kumar et al., 2014) and flood forecasts (Wanders et al., 2014; Alfieri et al., 2013). At continental and global scale land surface models (Balsamo et al., 2015; Reichle et al., 2011; Dirmeyer et al., 2006) and satellite sensors (Mecklenburg et al., 2016; Wagner et al., 2013; Entekhabi et al., 2010; Kerr et al., 2010) provide reliable estimates of soil moisture. The Advanced Scatterometer (ASCAT) sensors on board the Metop satellite series have been providing continuous active microwave measurements at C-Band (5.255 GHz) since 2006. ASCAT surface soil moisture products are produced operationally, at resolutions of 50 km and 25 km, by EUMETSAT and made available for Numerical Weather Prediction Centers. Passive microwave at L-band (1.4 GHz) are highly sensitive to surface soil moisture and they are used for soil moisture dedicated missions. It was first demonstrated with the Skylab mission which provides nine overpasses of L-band observations, at a resolution of 110 km, from 1973 to 1977 (Eagleman and Lin, 1976). The European Space Agency (ESA) Soil Moisture and Ocean Salinity (SMOS) mission was launched in 2009. SMOS was specifically designed for soil moisture measurements from space. Its concept relies on measurements of multi-angular fully polarised passive microwave emission of the Earth at L-band (1.4 GHz). SMOS brightness temperature observations have a resolution of about 40 km. These observations have been available in Near Real Time (NRT) since 2010. In 2016 a NRT level2 soil moisture product has been developed and implemented based on a neural network soil moisture retrieval approach (Muñoz Sabater et al., 2016; Rodriguez et al., 2016, 2017). The NRT soil moisture product is of great interest for operational hydrology application in particular. Following SMOS, the National Aeronautics and Space Administration (NASA) Soil Moisture Active Passive (SMAP) mission (Entekhabi et al., 2010), was launched in January 2014. SMAP uses a rotating antenna, which takes measurements at a single incidence angle. The concept of SMAP is based the combination between active and passive observations to produce high resolution (9 km) soil moisture estimates from Space. After the active sensor of SMAP failed in July 2014, it was decided to use the Sentinel-1 radar observations at C-band for the active component of the SMAP mission.

*Corresponding author
[1]Now at CNRM UMR 3589, Météo-France/CNRS, Toulouse, France

Several operational centres started to investigate the use of L-band passive microwave brightness temperature observations from SMOS and SMAP for Numerical Weather Prediction (NWP) applications (Muñoz Sabater et al., 2018a,b; Carrera et al., 2015). At ECMWF the SMOS data has been passively implemented in the Integrated Forecasting System for monitoring purpose (Muñoz Sabater et al., 2011b). In these systems a forward operator is used to simulate the brightness temperature as seen from space, so that the modelled and the observed brightness temperatures provide the basis to monitoring and data assimilation. The Community Microwave Emission Modelling platform was developed as low frequency passive microwave operator (Holmes et al., 2008; de Rosnay et al., 2009a,b; Drusch et al., 2009). Drusch et al. (2009) conducted a first evaluation the ECMWF forward simulation by comparing ERA-40-based L-band brightness temperature with the historic Skylab observations (S-194 radiometer). Their study was preliminary, limited by the number of observations and the coarse resolutions of the observations and the ERA-40 reanalysis. However it allowed to show that he choice of parameterisations used in CMEM to account for vegetation opacity or soil roughness has a strong influence on the simulated brightness temperature. The authors showed that the simple parameterisation of Kirdyashev et al. (1979) for the vegetation opacity model provided TB in best agreement with the Sklab observations. de Rosnay et al. (2009a) used the Advanced Microwave Scanning Radiometer - Earth Observing System (AMSR-E) C-band brightness temperature observations over West Africa to evaluate CMEM for different combinations corresponding to 12 configurations of the soil dielectric model, soil roughness model and vegetation opacity model. More recently the capacity of the Variable Infiltration Capacity model coupled to CMEM was evaluated against SMOS L-Band observations over the upper Mississippi basin for 2010-2011 (Lievens et al., 2015).
This paper has three objectives. The first one is to evaluate different combinations of CMEM parameterisations against SMOS observations in order to define CMEM's configuration for SMOS monitoring and data assimilation in the ECMWF Integrated Forecasting System (IFS). The second objective is to present and to evaluate the multi-angular seasonal bias correction approach developed to use SMOS data at ECMWF. The third objective is to provide long term monitoring statistics of SMOS observations for the period covering 2010-2016.

Section 2 presents the data and methods used in this paper. It describes the SMOS data, the ECMWF IFS and the CMEM forward operator. It also presents the microwave models inter-comparison methods and the multi-angular seasonal bias correction approach that was developed for SMOS. Section 3 presents results. It includes discussions on the results of the microwave models inter comparison results, the bias correction results and the 7 year SMOS monitoring statistics against the ERA-Interim based forward brightness temperature from ECMWF. Section 4 concludes the paper.

2. Data and Methods

2.1. SMOS brightness temperature observations

SMOS is the first satellite mission designed for soil moisture measurements from space (Kerr et al., 2010, 2012; Mecklenburg et al., 2016). It provides 2D-interferometric measurements of multi-angular and full polarisation brightness temperatures at L-band (1.4GHz) with a spatial resolution of 35 km to 50 km. At ECMWF the operational Near Real Time (NRT) level 1 brightness temperature product of SMOS is used. It is available within three hours of sensing, which is suitable for operational Numerical Weather Prediction applications. For this study we used the consistent reprocessed and operational level1 brightness temperature products from the SMOS processor v5.05 from January 2010 to March 2012 and from April 2012 to April 2015, respectively. From May 2015 to December 2016 the operational SMOS NRT brightness temperature from the processor version 6.20 was used.

Brightness temperature data at XX and YY polarisations at the antenna frame are used in this study. Observations at incidence angles of 30°, 40° and 50° were pre-processed by applying a noise filtering using a 2° binning angle, as described in Muñoz Sabater et al. (2014). Quality control based on the NRT v5.05 product flag information was applied to ensure that only the Alias Free Field of View data is used for this study (SMOS information flag, code 025144, bit 5). We also discarded observations which are flagged to be affected by Radio Frequency Interferences (RFI, indicated by bit number 1 and 4 of the same information flag), as well as observations with unrealistic brightness temperature values lower than 150 K or larger than 330 K. SMOS observations are discarded for pixels with fraction of water bodies larger than 5% (code 013048 in the NRT product) or with radiometric accuracy exceeding 4 K (parameter code 012080).

The SMOS brightness temperature observations were interpolated, using a bi-linear interpolation approach, to the ECMWF Gaussian Reduced model grid at 80km resolution (TL255) for the inter comparison study, and at 40km (TL511) for the bias correction and for the SMOS long term monitoring and comparison with ERA-Interim based brightness temperatures for 2010-2016 (see Sections 2.4 for the experiments description).

2.2. ECMWF Land surface model

H-TESSEL (Hydrology-Tiled ECMWF Scheme for Surface Exchanges over Land) is the land surface model used in the ECMWF Integrated System (Balsamo et al., 2009; Viterbo and Beljaars, 1995). It is a point-wise land surface model, which represents the vertical soil water movements by solving the Richard's equation (Richards, 1931) over four soil layers of 7 cm, 21 cm, 72 cm and 1.89 m thickness from top to bottom of the root zone. The surface runoff is based on the variable infiltration capacity (Balsamo et al., 2009). The soil texture is accounted for using the Food and Agriculture Organisation (FAO) Digital Soil Map of the World (DSMW) (FAO, 2003). H-TESSEL land use classification follows the Global Land Cover Characteristics (GLCC) data (Loveland et al., 2000), with assigned dominant high and low vegetation types. Land cover heterogeneities are represented using a tile approach, with up to seven tiles in each grid box of the model: bare soil, low vegetation, high vegetation, interception and two tiles for

snow (exposed and shaded snow) as described in Dutra et al. (2010). The vegetation annual cycle is accounted for using a monthly Leaf Area Index climatology (Boussetta et al., 2013).

H-TESSEL is fully coupled to the atmosphere for NWP applications, as well as for the ERA-Interim reanalysis (Dee et al., 2011). ERA-Interim provides global reanalysis of the land and the atmosphere, from 1979 to present. It is produced at a resolution of 80 km (TL255 spectral resolution), with a delay of about one month from NRT. In the past years a land surface model reanalysis, called ERA-Interim/Land was developed by running the land surface model forced by the ERA-Interim forcing conditions with precipitation corrected by the Global Precipitation Climatology Project data from 1979 to 2010 (Balsamo et al., 2015). ERA-Interim/Land was produced at the same resolution than ERA-Interim, but using an up-to-date version of the land surface model (IFS cycle 38R1). The ERA-Interim/Land soil moisture reanalysis was evaluated against in situ soil moisture measurements by Albergel et al. (2013), showing good performance of the land reanalysis to capture soil moisture variabilities at time scales ranging from daily scale to seasonal and inter-annual scales.

In this paper, we use a global land-reanalysis produced by forcing H-TESSEL, cycle 41R1, by ERA-Interim atmospheric conditions at a resolution of TL511 (40km), which is the Gaussian reduced grid closest to the SMOS resolution. H-TESSEL simulations were conducted for the period from 2010 to 2016, providing input land surface conditions, including soil moisture and temperature at different model depth, soil temperature, air temperature, vegetation characteristics, to CMEM.

2.3. The Community Microwave Emission Modelling Platform

CMEM is the forward operator used at ECMWF for low frequency passive microwave brightness temperatures observations monitoring and data assimilation (de Rosnay et al., 2009a; Drusch et al., 2009; Holmes et al., 2008). It is a community model, developed and maintained by ECMWF. In this paper, the latest release of CMEM (v5.1) is described and results presented in section 3.1 define the default configuration of this CMEM release that has been used for operational monitoring and research developments of SMOS brightness temperature data assimilation (Muñoz Sabater et al., 2018b). CMEM is an open source code, freely available to the scientific community through the ECMWF web pages, with an Apache licence. It has been used by a number of research and operational centres as forward model for low frequency passive microwave applications (Muñoz Sabater et al., 2018a; Carrera et al., 2015; Lievens et al., 2015).

For each model grid point, CMEM computes the Top-of-Atmosphere (TOA) brightness temperature for each polarisation p (h or v for horizontal or vertical), and for each incidence angle θ, as the sum of the ascending atmospheric emission ($T_{Bau,p}$) and the weighted sum the of the brightness temperature computed at the top the vegetation, $T_{Btov,p}(i)$, of each individual land surface model tile (i = 1 to 7, see section 2.2 above):

$$T_{Btoa,p,\theta} = T_{Bau,p,\theta} + exp(-\tau_{atm,p,\theta}) \cdot \sum_{i=1}^{7} f(i) \cdot T_{Btov,p,\theta}(i) \quad (1)$$

where $\tau_{atm,p,\theta}$ the atmospheric optical depth, and $f(i)$ is the fraction coverage of each tile.

The brightness temperature at the top of the vegetation layer computed for each tile as:

$$T_{Btov,p,\theta} = T_{Bsoil,p,\theta} \cdot exp(-\tau_{veg,p,\theta}) + T_{Bveg,p,\theta}(1 + r_{r,p,\theta} \cdot exp(-\tau_{veg,p,\theta})) + T_{Bad,p,\theta} \cdot r_{r,p,\theta} \cdot exp(-2 \cdot \tau_{veg,p,\theta}) \quad (2)$$

with $T_{BS\,oil,p,\theta}$, $T_{BVeg,p,\theta}$ and $T_{Bad,p,\theta}$ the brightness temperature of the soil, vegetation and downward atmospheric components, respectively; $r_{r,p,\theta}$ the rough soil surface reflectivity (also expressed as one minus the emissivity $e_{r,p,\theta}$), and $\tau_{veg,p,\theta}$ the vegetation optical depth at polarisation p and incidence angle θ.

CMEM is composed of four modules to compute the contributions from the soil, vegetation, snow and atmosphere to the TOA brightness temperature. It includes a choice of different parameterizations for each component of the modules as summarised in Table 1.

[Table 1 about here.]

2.3.1. CMEM soil module

In the soil module, the dielectric mixing model is used to compute dielectric constant as a function of volumetric soil moisture, soil temperature, soil texture and microwave frequency. Three parameterizations are implemented in CMEM to infer the soil dielectric constant. The Dobson model is valid for frequency in a range of 1 GHz to 20 GHz (Dobson et al., 1985). The Mironov (Mironov et al., 2004) and the Wang and Schmugge (Wang and Schmugge, 1980) models are valid for frequencies between 1 GHz and 10 GHz. Results from de Rosnay et al. (2009a) over West Africa showed that the Wang and Schmugge model and the Mironov model perform better than the Dobson model at C-band. They account for the effect of bound soil water and they are more suitable for a large range of frequencies. The Mironov parameterization has been widely used for L-band applications at the field scale (Mialon et al., 2012, for example), and at global scale in particular in the SMOS retrieval algorithm (Kerr et al., 2016).

The soil brightness temperature is expressed, following the Rayliegh-Jeans approximation, as the product between the effective temperature T_{eff} and the soil emissivity $e_{r,p,\theta}$. A simple model was proposed by Choudhury et al. (1982) to approximate the effective as a function of the surface soil temperature (at $\sim$ 5 cm), soil temperature at depth (at $\sim$ 50 cm) and an empirical parameter C which depends on frequency. This parameterization was modified by Wigneron et al. (2001) for L-band radiometry including a dependency of C to soil moisture. Holmes et al. (2006) proposed a more complex parameterization where C is expressed as a function of the dielectric constant. Based on the long term SMOSREX data set, de Rosnay et al. (2006) provided an inter-comparison of these three parameterizations. The approximation from Wigneron et al. (2001) was shown to be well suited for global scale studies and it used as default configuration in CMEM to compute the soil effective temperature (de Rosnay et al., 2009a).

Soil roughness has a large impact on soil emission and reflectivity (Mialon et al., 2012; Escorihuela et al., 2007). Increase in surface roughness surfaces leads to higher emissivities and reduced difference between horizontally and vertically polarized brightness temperatures. CMEM includes five soil roughness parameterizations listed in Table 1),

and described in detail in Muñoz Sabater et al. (2011a). They are derived from the semi-empirical approach proposed by Wang and Choudhury (1981) to represent soil roughness effects on the microwave emission. The rough emissivity is computed as a function of the smooth emissivity $r_{s,q,\theta}$ and three parameters Q, h, N:

$$r_{r,p,\theta} = \left(Q \cdot r_{s,q,\theta} + (1 - Q) \cdot r_{s,p,\theta}\right) \cdot exp\left(-h \cdot cos^N\theta\right) \tag{3}$$

where p and q refer to the polarization states, Q is the polarization mixing factor, N is a parameter that describes the angular dependence, h is the roughness parameter and θ the incidence angle. The mixing factor Q is considered to be very low at low frequencies and is generally set to 0 (Wigneron et al. (2007); Njoku et al. (2003)). Based on equation 3 two parameterizations have been proposed with $N = 0$ and the following computation for the h parameter:

$$h = (2k\sigma)^2 \ (Choudhury) \tag{4}$$

$$h = 1.3972 \cdot (\sigma/L_c)^{0.5879} \ (Wsimple) \tag{5}$$

where k is the wave number and L and σ are correlation length and standard deviation of surface roughness. Other soil roughness parameterizations account for the dependency of the roughness parameter on soil moisture and soil texture (ATBD (2007)), or for both soil moisture and vegetation type with N depending on vegetation and polarization (Wigneron et al. (2007)). Wegmüller and Mätzler (1999) uses a single roughness parameter $h = k \cdot \sigma$. In this paper the parameterizations developed for L-band applications, as well as the simple Choudhury et al. (1979) model are used and evaluated against the SMOS observations as indicted in bold in Table 1.

2.3.2. CMEM vegetation module

The vegetation layer is represented in CMEM following the so-called $\tau - \omega$ approach. As formulated in Equation 2, vegetation contributes in several ways to the measured signal at the top of the atmosphere. It attenuates the soil emission, it attenuates the downward atmospheric emission and the upward atmospheric emission after it was reflected on the soil surface, and it has a direct contribution to the signal expressed as:

$$T_{Bveg,p} = T_c \cdot (1 - \omega_p) \cdot (1 - exp(-\tau_{veg,p})) \tag{6}$$

where T_c is the canopy temperature and ω_p is the single scattering albedo at polarization p. CMEM include a choice of four parameterisations to account for the vegetation effect on the signal. They differ in the approach used to compute the vegetation optical depth as described in details in a number of papers including for example (de Rosnay et al., 2009a; Drusch et al., 2009; Wigneron et al., 2007). The parameterizations from Wigneron et al. (2007) and Jackson and O'Neill (1990), are suitable at L-band. The Kirdyashev et al. (1979) and Wegmüller et al. (1995) models account for the wave number in their parameterisation of the optical depth. They are applicable for a larger range of frequencies. In this paper CMEM performances are compared and evaluated against SMOS data, for different configurations using the parameterizations of Wigneron et al. (2007), Jackson and O'Neill (1990), and Kirdyashev et al. (1979).

2.3.3. CMEM snow and atmospheric modules

In the case of presence of snow, CMEM accounts for a snow layer as described in Holmes et al. (2008) with the snow reflectivity computed using the single layer version of the Helsinki University of Technology (HUT) model (Pulliainen et al., 1999). In this study the snow covered areas are filtered out in the quality control as described in the next subsection.

In the atmospheric module of CMEM, the atmosphere optical thickness $\tau_{atm,p}$ is computed following the parameterisation developed by Pellarin et al. (2003).

2.3.4. Faraday rotation

CMEM as described above simulates TOA brightness temperature in the Earth reference frame at both horizontal and vertical polarisations. These brightness temperature need to be transformed into the SMOS antenna frame to be compared to the SMOS data. The transformation of CMEM's $T_{Btoa,h}$ and $T_{Btoa,v}$ into the SMOS antenna frame accounts for the SMOS geometry and to the Faraday rotation in the ionosphere as described in ATBD (2007). In dual polarisation mode, the transformation of brightness temperature is expressed as follow:

$$\begin{bmatrix} T_{Becm,xx,\theta} \\ T_{Becm,yy,\theta} \end{bmatrix} = \begin{bmatrix} cos^2(a) & sin^2(a) \\ sin^2(a) & cos^2(a) \end{bmatrix} \begin{bmatrix} T_{Btoa,h,\theta} \\ T_{Btoa,v,\theta} \end{bmatrix} \tag{7}$$

where a is the total rotation angle computed as sum if the geometric and the faraday rotation angles. This transformation is included as a CMEM post-processing step in the ECMWF IFS. In the following of the paper, we use $T_{Becm,xx,\theta}$ and $T_{Becm,yy,\theta}$ from CMEM to compare with the SMOS brightness temperature data in the antenna frame.

2.4. Numerical experiments

A series of numerical experiments were conducted with CMEM, using the H-TESSEL land surface model input, to address the three objectives of this paper. To identify CMEM's bests configurations, 36 different CMEM configurations, corresponding to different combinations of three dielectric models, three vegetation opacity models and four roughness models presented in Table 1, were evaluated against SMOS brightness temperature observations. Due to the large number of experiments, this set was limited to 40° incidence angle and it was conducted at a resolution of TL255 (80 km) for a two-year period (2010-2011). To develop the bias correction, the selected best CMEM configuration was used and numerical experiments were conducted at three different incidence angles, 30°, 40° and 50°, at a resolution of TL511 (40km), which is close to the SMOS resolution, for 2010-2013. The 40° experiment was extended for 2014-2016 for long term monitoring purpose. Table 2 summarises the experiments conducted for each objective. It also indicates the version of the SMOS processor used to produce the SMOS data compared to the ERA-Interim based CMEM forward brightness temperatures, and it indicates in which section the results are presented.

[Table 2 about here.]

In addition to the quality control described in Section 2.1, which was based on the SMOS product quality flags, we used the reanalysed land surface conditions from H-TESSEL from each experiment to discard model and observation values for grid points with presence of snow, and grid points with air temperature lower than 273 K. We also discarded areas with complex topography with a slope larger than 4%, and areas with water fraction larger than 5%.

2.5. Bias correction method

SMOS brightness temperature observations are used at ECMWF for monitoring and for data assimilation to initialise the NWP system (Muñoz Sabater et al., 2018b). A key assumption for data assimilation is that model and observations are unbiased, with random zero-mean errors (Yilmaz and Crow, 2013; Dee, 2005). However, in reality, systematic differences exist between modelled and observed radiances. They are caused by a number of reasons such as problems with the data, representativeness issues, forward model approximations, simplified representation of the processes. So, it is of crucial importance to correct for the systematic errors between the model and the observations prior to data assimilation. Cumulative Distribution Function matching (CDF-matching) allows to match the statistical moments of the data to the model ones (Reichle and Koster, 2004) and it has been used in different forms for a number of studies (Lievens et al., 2015; Draper et al., 2012; Scipal et al., 2008, for example). As pointed out by Draper et al. (2012) there are also systematic differences between the seasonal cycles of model and observations. Not accounting for these seasonal scale systematic discrepancies would affect the matching at both short time scales and seasonal scale.

In this paper we use a point-wise, multi-angular and monthly rescaling approach to remove the seasonally varying systematic biases between the SMOS observations and the ECMWF CMEM forward simulations. We use the 4-year (2010-2013) observations and forward simulations, at 40 km resolution of experiments of Set 2 (Table 2). Using a 3-month moving window, we compute the 4-year averaged statistical moments (mean and variance) of the observed (T_{Bsmos}) and simulated (T_{Becm}) brightness temperatures for each grid point, for each calendar month from January to December, at each polarisation, and for each incidence angle. A minimum of 50 model and observations values per angle, polarisation and moving window remaining after quality control (sections 2.1 and 2.4) is required to compute the moments. The statistical moments are then used to compute monthly maps of CDF-matching parameters (A,B) at xx and yy polarisations, for 30°, 40° and 50° incidence angles, as follow:

$$A = < T_{Becm} > - < T_{Bsmos} > \cdot \frac{StDev(T_{Becm})}{StDev(T_{Bsmos})} \tag{8}$$

$$B = \frac{StDev(T_{Becm})}{StDev(T_{Bsmos})} \tag{9}$$

The first parameter, A, is considered as a bias correction parameters and the second parameter, B, as a rescaling parameter. They are used to transform the observed SMOS observations for assimilation purposes as:

$$T^{\star}_{Bsmos} = A + B \cdot T_{Bsmos} \tag{10}$$

The obtained matching parameters and results of the seasonal bias correction approach are presented in section 3.2.

3. Results

3.1. CMEM global intercomparison

Figure 1 shows maps of 2010-2011 mean brightness temperatures at xx and yy polarisations, (a) as observed from SMOS and (b) simulated from one of the experiments of Set 1 - the one using Wang for the dielectric model, Wsimple roughness and Wigneron for the vegetation (see Tables 1 and 2). Figure 1c shows the mean first guess departure (observation minus model) brightness temperature at each polarisation, and Figure 2 shows, maps of root mean square error (RMSE), unbiased RMSE (uRMSE) and correlation for the same period and experiment. Mean values of SMOS brightness temperature at xx polarisation typically range between 240 K and 280 K in most areas (Figure 1a), with colder mean brightness temperatures at high latitude. As expected, measured SMOS brightness temperatures are larger at yy than at xx polarisation, in particular over warm desert areas with up to 300 K mean values for 2010-2011. Figure 1(b,c) show that forward simulations using this configuration of CMEM tend to overestimate brightness temperature values at both xx and yy polarisations by up to 20 K, specially in dry areas, but also in North America and India, and to underestimate them over tropical forest areas and at high latitudes.

[Figure 1 about here.]

The top panel of Figure 2 shows relatively large RMSE values often between 16 K and 30 K at xx and yy polarisations matching relatively well areas with large bias shown in Figure 1(c). Maps of uRMSE, Figure 2(b), show lower values than for RMSE, indicating the large contribution of the bias to the RMSE for this configuration of CMEM. Areas with uRMSE larger than 16K remain in Asia, Eastern Europe. These areas are known to be affected by Radio Frequency Interference (RFI) sources leading to unreliable SMOS measurements. The RFI contamination is not systematically captured in the RFI flag, explaining large uRMSE in these regions despite the quality control applied as described in the previous section. The bottom panel of Figure 2 shows that SMOS measurements and CMEM forward simulations are well correlated for 2010-2011, with values larger than 0.4 in most areas. Lowest correlation values are shown in grey in tropical forests areas. They are due to the relative stable brightness temperatures in these areas, with low temporal dynamics in both the model and the observations, leading to low correlation. Low correlation values are also shown in RFI affected areas of Asia. Global mean statistics for this configuration of CMEM indicate correlation values of 0.57 and 0.53 at xx and yy polarisation, respectively. Values of uRMSE are 11.63 K and 11.49 K.

[Figure 2 about here.]

[Table 3 about here.]

[Table 4 about here.]

Global mean 2010-2011 statistics are provided in Tables 3 and 4 for each of the 36 experiments of Set 1 corresponding to different configurations of CMEM. They include correlation, uRMSE and bias and SDV, which is the normalised standard deviation, i.e the ratio between the simulated and observed brightness temperature standard deviations. The results of these two Tables are also summarised in Taylor diagrams (Taylor and Clark, 2001) in Figure 3 and the annual cycles of uRMSE and correlation statistics are shown in Figure 4.

In this paper, the primary criteria of evaluation to select best CMEM parameterizations are correlation and uRMSE metrics, whereas bias and SDV results are secondary criteria. This is because Numerical Weather Prediction applications, including monitoring and assimilation, apply an a priori a bias correction to match the mean and the variance of model and observed brightness temperatures (Section 2.5).

Results of Tables 3 and 4 and Figures 3 all clearly show that the choice of the roughness parameterisation has the largest impact on correlation, uRMSE, bias and SDV statistics. Wtexture generally shows poorer correlation and uRMSE performances than the other parameterisations. Figure 4 shows that this result is persistent accros the annual cycle. Results form the two tables and the Taylor diagrams show however that experiments using Wtexture best capture the SMOS brightness temperature standard deviation, with SDV values close to 1. The other roughness parameterisations lead to SDV values lower than 1, indicating that they underestimate the variance compared to the SMOS data. The forward model is based on the 7 cm top soil layer of H-TESSEL, which is in most situations larger than the SMOS sensing depth. In turn, the SMOS data with a shallower sensing depth is expected to capture larger standard deviation, related to highly variable surface soil moisture, than the model, which explains that most roughness models underestimate SDV. The Wigneron and Wsimple roughness parameterisations better match the SMOS data than Wtexture or Choudhury in terms of correlation, uRMSE and bias. And looking into more details at the Wsimple and Wigneron statistics, results show that Wsimple has lower uRMSE and larger correlation than Wigneron.

For the vegetation optical depth, statistics presented in Tables 3 and 4 show that Jackson and Wigneron perform better than Kirdyashev in terms of correlation and uRMSE. This result differ from the ALMIP-MEM results of de Rosnay et al. (2009a) who showed that Kirdyashev was performing better than Jackson or Wigneron at C-band over West Africa. Result obtained here at L-band are not surprising as Jackson and Wigneron parameterisations were developed for L-band, so they are best suited for SMOS applications, whereas Kirdyashev is a multi-frequency model. The Wigneron parameterisation tend to show slightly better statistics than Jackson in terms of uRMSE.

Simulated brightness temperatures are less sensitive to the dielectric model than to the vegetation opacity and soil roughness models. The Wang and Schmugge and the Mironov soil dielectric models perform similarly and lead to a slightly better agreement with SMOS observations than the Dobson dielectric model. Either of them could be used for ECMWF NWP applications. In this paper the Wang and Schmugge model is selected to be used.

Based on this intercomparison the configuration of CMEM retained for ECMWF SMOS forward modelling activities is the one based the Wang and Schmugge dielectric model, the Wigneron simple roughness model and the Wigneron vegetation model. This combination of CMEM options also defines the CMEM v5.1 default configuration which was released by ECMWF based on these results.

[Figure 3 about here.]

[Figure 4 about here.]

3.2. Bias correction results

Figures 5 and 6 show the maps of CDF-matching parameters at xx polarisation, for 30°, 40° and 50° incidence angles, for January and July, respectively, using the 2010-2013 data sets (see Table 2). Both the bias correction term A and the rescaling term B show a relatively good consistency accross the different incidence angles. The bias correction parameter A has generally positive values in desert areas, in particular in Sahara and Australia, which are consistent with the departure results presented at 40° in Figure 1 for 2010-2011 at coarser resolution. In January, Figure 5 shows that large areas in the northern hemisphere do not have any CDF-matching parameters due quality control rejecting frozen and snow covered areas in the winter hemisphere. In both January and July, areas with complex topography (e.g. in the US Rocky mountains, The Andes, the Alpes and parts of the Himalayan mountains) are masked out. The Figures also show that regions in China are masked out, which is due to RFI filtering.

These CDF-matching parameters are applied to the ERA-Interim based CMEM forward simulations conducted for 2010-2013 for experiments Set 2 as detailed in Section 2. Figure 7 shows maps of RMSE and mean difference between SMOS observations and ECMWF CMEM forward simulations at 40° incidence angle, for 2013 computed before (left) and after (right) CDF-matching. Before CDF-matching, RMSE values typically range between 16 K and 20 K (red colours). After bias correction RMSE values are in the range of 4 K to 8 K in most areas. The mean bias is also reduced to a residual value lower than 1 K in most areas. Figure 8 presents maps of correlation and standard deviation before and after bias correction. The top-left panel of Figure 8 indicates very good correlation values between SMOS observations and CMEM even before bias correction. In North America and in parts of Australia, correlation values larger than 0.8 dominate. The bias correction, because it relies on a monthly approach, further improves the agreement between the SMOS observations and CMEM at the seasonal scale, leading to increased correlation values after bias correction (top right of Figure 8).

[Figure 5 about here.]

[Figure 6 about here.]

[Figure 7 about here.]

[Figure 8 about here.]

[Figure 9 about here.]

[Figure 10 about here.]

Figure 9 shows the CDF of brightness temperatures at xx polarisation (left) and yy polarisation (right), at 40° incidence angle for ECMWF CMEM forward simulations (blue), SMOS observations before bias correction (red) and SMOS observations after bias correction (green). It shows that the multi-angular polarised monthly CDF matching approach allows to effectively match the cumulative distributions of the observed and simulated brightness temperatures.
Figure 10 gives detailed examples of time series and CDF of ECMWF CMEM simulations and SMOS observations before and after bias correction in two areas of Australia (25S-35S; 140E-150E), and South America (15S-20S;50W-45W). The time series shown in the top panel of Figures 10, in Australia, shows that the SMOS observations before bias correction (red) are colder that the ECMWF CMEM forward simulations, as already pointed out with the global maps shown in Figure 7. It also shows that the annual cycle and the shorter time scale variability are captured by the observations and the model (as shown in Figure 8 for this area). There are several occurrences of strong decrease in brightness temperature, typically corresponding to precipitation events and increased soil moisture, observed and simulated around day 25 and 60 and 145. It is clear from this figure that the SMOS observations have a larger variability than the model forward simulations as expected and as discussed in the previous subsection, due to a shallower SMOS sampling depth than the ECMWF model top layer thickness. For example on days 90 and 145, the amplitude of the SMOS signal is larger than that of ECMWF. On a single event it could be attributed to a number of reasons, such as for example a lack of precipitation in the ECMWF system leading an underestimation of soil moisture increase. However, the fact that the SMOS variability is systematically larger than the ECMWF CMEM forward simulations is consistent with the model layer and SMOS sampling depth mismatch. One of the purpose of bias correction is specifically to correct for model approximations than lead to systematic differences (Dee, 2005). The green curve of the top panel of Figure 10 shows that after bias correction, the SMOS data is in general better agreement with the model at the seasonal scale with remaining differences at the daily scale and precipitation event scale which are of potential relevance for data assimilation purpose. In South Americia (bottom panel of Figure 10) the observed and simulated brightness temperature are already in relatively good agreement before bias correction, both in term of mean value and variability. For both regions of Figure 10, the right panels show that the CDF are efficiently matched at the regional scale.

Figures 11 and 12 show histograms of global scale SMOS first guess departure (observations minus model) before and after bias correction, for different incidence angles at xx polarisation and yy polarisation, for the months of January 2013 and July 2013, respectively. Before bias correction (in red) they show uncentered distributions with a relatively large spread, which illustrate systematic differences between the observations and the model at all incidence angles and polarisations. The monthly bias correction (in green) leads to narrow and centred first guess departure distributions. A yearly bias correction, based on CDF matching parameters that would be computed on yearly statistical moments of SMOS and ECMWF brightness temperatures, is also illustrated (in yellow) in the Figure. It shows that the obtained first guess departure distribution would have a larger spread than with the monthly bias correction,

demonstrating the benefit of the seasonal approach.

[Figure 11 about here.]

[Figure 12 about here.]

Tables 5 and 6 give an overview of the yearly statistics of the ECMWF CMEM forward simulations and the SMOS brightness temperatures observations for each incidence angle, each polarisation for 2010, 2011, 2012 and 2013. Table 5 shows that, before bias correction, depending on the incidence angle and the year, RMSE values range between 16.96 K and 20.64 K at xx polarisation and between 12.77 K and 17.30 K at yy polarisation, with mean value for all polarisations and incidence angles of of 16.67 K. Global mean bias are mostly negative, between -7.16 K and -0.64 K at xx polarisation and between -2.74 K and 0.5 K at yy polarisation. The multi-angle multi-polarisation bias is -2.097 K. These mean statistics hide large spatial scale differences as shown in Figure 7 and 8. Correlation values are on average 0.56, varying between 0.51 and 0.60 at xx polarisation, and between 0.49 and 0.64 at yy polarisation, with large confidence interval for each angle, polarisation and year. Anomaly correlations are computed based on time series obtained by removing the seasonal cycle based on a 4-month moving window with an averaged value of 0.31. After bias correction, the mean correlation, RMSE and bias are improved to 0.62, 9.91 K and 0.0016 K, respectively. The anomaly correlation remain very close to its value before bias correction, 0.31 K, which is as expected since the seasonal bias correction approach preserves the SMOS signal short term variability.

[Table 5 about here.]

[Table 6 about here.]

3.3. Long term SMOS monitoring

Figure 13 shows long term global scale monitoring statistics obtained at a 40° incidence angle, from 2010 to 2016 using the ERA-Interim-based CMEM forward simulations of Set 3 described in Table 2 and the SMOS brightness temperature measurements for the entire period as described in Section 2.1. The left panel shows that at both polarisations, correlations and anomaly correlation statistics steadily improve between 2010 and 2016. The correlation values increase from 0.57 to 0.63 at xx polarisation and from 0.53 to 0.63 at yy polarisation, respectively. The anomaly correlation values also increase from 0.34 to 0.40 and from 0.27 to 0.37 at xx and at yy polarisations. The right panel shows that the RMSE and uRMSE values decrease from 2010 to 2016 at both polarisations. The RMSE values range from 18.62 K in 2010 to 17.12 K in 2016 at xx polarisation and from 16.27 K to 13.57 K at yy polarisation. For the uRMSE, the results show an improvement from 11.82 K to 10.46 K and from 11.75 K to 9.25 K at xx and yy polarisations, respectively. These results are based on reanalysis based forward simulations, which are expected to be of

constant quality. Consistent SMOS brightness temperatures from the SMOS processor v5.05 are used until April 2015 and from the SMOS processor v6.20 after May 2015 (Section 2.1). So, the steady improvement shown from 2010 to 2014 is entirely due to SMOS observations improvement, possibly due to actions taken to manage RFI contamination (Mecklenburg et al., 2016; Kerr et al., 2016). Improvements for 2015-2016 result from combined SMOS processor improvements and possible RFI contamination decrease. Although the different contributions are difficult to disentangle these results clearly show an overall SMOS brightness temperature product quality substantial improvement at both polarisations between 2010 and 2016.

[Figure 13 about here.]

4. Summary and Conclusion

This paper presented the SMOS forward modelling activities conducted at ECMWF to use the SMOS brightness temperature data.

The first objective of the paper was to evaluate different combinations of CMEM parameterisations against SMOS observations and to define CMEM's configuration for SMOS monitoring and data assimilation activities at ECMWF. To identify the best configuration of CMEM, 36 numerical experiments, using different combinations of three dielectric models, three vegetation opacity models and four roughness models, were conducted at 80 km resolution and at 40° incidence angle for 2010-2011. Experiments were conducted using ERA-Interim conditions as input of the land surface model H-TESSEL and the forward model CMEM. Results were evaluated against SMOS brightness temperature observations at both polarisations. Results show that simulated brightness temperatures are most sensitive to the soil roughness models and least sensitive to the dielectric model. Best configurations of CMEM are shown to be those using the so-called Wigneron vegetation opacity model with the simple empirical Wigneron soil roughness model. The Wang and Schmugge and the Mironov soil dielectric models perform similarly and lead to better agreement with SMOS observations than the Dobson dielectric model. Based on this intercomparison the configuration of CMEM retained for ECMWF SMOS forward modelling activities is the one based the Wang and Schmugge dielectric model, the Wigneron simple roughness model and the Wigneron vegetation model.

The second objective of the paper was to present and to evaluate the SMOS bias correction approach developed to use SMOS brightness temperature data at ECMWF. The paper described a multi-angular multi-polarised monthly Cumulative Distribution Function bias correction based on SMOS and ECMWF re-analysed (ERA-Interim based) brightness temperatures for the period from 1 January 2010 to 31 December 2013. Experiments were conducted at 40 km resolution with and without bias correction and results were compared to the SMOS observations at global scale and at regional scale. Results show that the seasonal multi-angular multi-polarisation CDF-matching approach efficiently corrects for systematic differences between observations and model, with global root mean square differences (RMSD) and global mean bias for 2010-2013 for 30°, 40°, 50° incidence angles decreasing from 16.7 K and -2.1

K before bias correction to 7.91K and 0.0016 K after bias correction, respectively. The monthly approach allows to correct for seasonal cycles systematic differences, with correlation values improved from 0.56 before bias correction and 0.62 after bias correction. Residual differences remaining after bias correction correspond to random differences between the model and observations which provide relevant information for monitoring and data assimilation purposes.

The third objective of this paper was to provide long term monitoring statistics of SMOS observations for an extended period covering 2010-2016, focusing on 40° incidence angle data. Results of the comparison with reanalysis-based forward simulations were presented in terms of RMSD, uRMSD, correlation and anomaly correlation statistics. They consistently show that SMOS and ECMWF reanalysis-based brightness temperatures agreement steadily improves between 2010 and 2016, pointing out improvements of level 1 SMOS brightness temperature products quality through the SMOS lifetime. The improvement shown from 2010 to 2014 relies on a consistent SMOS processor version and reanalysed ECMWF brightness temperatures of constant quality. So, it is entirely due to SMOS observations improvement, possibly due to actions taken to manage RFI contamination. Improvements for 2015-2016 result from combined SMOS processor improvements and possible RFI contamination decrease. These results nevertheless clearly show an overall substantial quality improvement SMOS brightness temperature product at both polarisations between 2010 and 2014 and between 2015 and 2016.

The forward modelling results and bias correction results presented in this paper demonstrate the relevance of the SMOS observations for numerical weather prediction applications. Long term monitoring results also open perspectives for SMOS data assimilation studies for environmental systems monitoring, prediction and long term reanalyses.

Albergel, C., Dorigo, W., Reichle, R. H., Balsamo, G., de Rosnay, P., Muñoz Sabater, J., Isaksen, L., de Jeu, R., and Wagner, W. (2013). Skill and Global trend analysis of soil moisture from reanalyses and microwave remote sensing. *J. Hydrometeo*, 14:1259–1277. doi:10.1175/JHM-D-12-0161.1.

Alfieri, L., Burek, P., Dutra, E., Krzeminski, B., Muraro, D., Thielen, J., and Pappenberger, F. (2013). GloFAS global ensemble stream- flow forecasting and flood early warning. *Hydrology and Earth System Sciences*, 17:1161–1175. doi:10.5194/hess-17-1161-2013.

ATBD, S. (2007). SMOS Expert Support Laboratories, SMOS level 2 Processor for Soil Moisture Algorithm Theoretical Based Document (ATBD). *SO-TN-ESL-SM-GS-0001, issue 2.a*, page 124.

Balsamo, G., Albergel, C., Beljaars, A., Boussetta, S., Cloke, H., Dee, D., Dutra, E., Muñoz Sabater, J., Pappenberger, F., de Rosnay, P., Stockdale, T., and Vitart, F. (2015). ERA-Interim/Land: A global land water resources dataset. *Hydrology and Earth System Sciences*, 19:389–407. doi: 10.5194/hess-19-389-2015.

Balsamo, G., Viterbo, P., Beljaars, A., van den Hurk, B., Hirsch, M., Betts, A., and Scipal, K. (2009). A revised hydrology for the ECMWF model: Verification from field site to terrestrial water storage and impact in the Itegrated Forecast System. *J. Hydrometeo*, 10:623–643.

Boussetta, S., Balsamo, G., Beljaars, A., and Jarlan, L. (2013). Impact of a satellite-derived Leaf Area Index monthly climatology in a global Numerical Weather Prediction model. *Int J. Remote Sens.*, 34:3520–3542.

Carrera, M., Bèlair, S., and B., B. (2015). The canadian land data assimilation system (caldas): Description and synthetic evaluation study. *J. Hydrometeo*, 16:1293–1314. doi:10.1175/JHM-D-14-0089.1.

Choudhury, B., Schmugge, T., Chang, A., and Newton, R. (1979). Effect of surface roughness on the microwave emission from soils. *J. Geophys. Res.*, pages 5699–5706.

Choudhury, B., Schmugge, T., and Mo, T. (1982). A parameterization of effective soil temperature for microwave emission. *J. Geophys. Res.*, pages 1301–1304.

de Rosnay, P., Drusch, M., Boone, A., Balsamo, G., Decharme, B., Harris, P., Kerr, Y., Pellarin, T., Polcher, J., and Wigneron, J.-P. (2009a). Microwave Land Surface modelling evaluation against AMSR-E data over West Africa. The AMMA Land Surface Model Intercomparison Experiment coupled to the Community Microwave Emission Model (ALMIP-MEM). *J. Geophys. Res*, 114. doi:10.1029/2008JD010724.

de Rosnay, P., Drusch, M., and Muñoz Sabater, J. (2009b). SMOS Global Surface Emission Model. *ECMWF ESA Contract Report*. ESA/ESRIN Contract 4000101703/10/NL/FF/fk, MS1 Technical Note - Part1.

de Rosnay, P., Drusch, M., Vasiljevic, D., Balsamo, G., Albergel, C., and Isaksen, L. (2013). A simplified Extended Kalman Filter for the global operational soil moisture analysis at ECMWF. *Quart. J. Roy. Meteorol. Soc.*, 139:1199–1213. doi: 10.1002/qj.2023.

de Rosnay, P., Wigneron, J.-P., Holmes, T., and Calvet, J.-C. (2006). Parameterizations of the effective temperature for L-band radiometry. Intercomparison and long term validation with SMOSREX field experiment, Radiative Transfer Models for Microwave Radiometry. *In Mätzler, C., P.W. Rosenkranz, A. Battaglia and J.P. Wigneron (eds.), "Thermal Microwave Radiation - Applications for Remote Sensing", IET Electromagnetic Waves Series 52, London, UK, Christian Matzler (Ed.), Product code: EW 052 ISBN: 0-86341-573-3 and 978-086341-573-*.

Dee, D. (2005). Bias and data assimilation. *Quart. J. Roy. Meteorol. Soc.*, 131:3323–3343.

Dee, D., Uppala, S., Simmons, A., Berrisford, P., Poli, P., Kobayashi, S., Andrae, U., Balsameda, M., Balsamo, G., Bauer, P., Bechtold, P., Beljaars, A., van de Berg, L., Bidlot, J., Bormann, N., Delsol, C., Dragani, R., Fuentes, M., Geer, A., Haimberger, L., Healy, S., Hersbach, H., Hólm, E., Isaksen, L., Kållberg, P., Köhler, M., Marticardi, M., McNally, A., Monge-Sanz, B., Morcrette, J.-J., Park, B.-K., Peubey, C., de Rosnay, P., Tavolato, C., Thépaut, J.-N., and Vitart, F. (2011). The ERA-Interim reanalysis: Configuration and performance of the data assimilation system. *Quart. J. Roy. Meteorol. Soc.*, 137:553–597. doi:10.1002/qj.828.

Dirmeyer, P. A., Gao, X., Guo, Z., Oki, T., and Hanasaki, N. (2006). The Second Global Soil Wetness Project (GSWP-2): Multi-model analysis and implications for our perception of the land surface. *Bull. Americ. Met. Soc.*, 87(10):1381–1397.

Dobson, M., Ulaby, F., Hallikainen, M., and EL-Rayes, M. (1985). Microwave dielectric behavior of wet soil-partii: Dielectric mixing models. *IEEE Trans Geosc. Sci*, 38:1635–1643.

Draper, C., Reichle, R., De Lannoy, G., and Liu, Q. (2012). Assimilation of passive and active microwave soil moisture retrievals. *Geophy. Res. Letters*, 39. L04401, doi:10.1029/2011GL050655.

Drusch, M. (2007). Initializing numerical weather prediction models with satellite-derived surface soil moisture: Data assimilation experiments with ECMWFs Integrated Forecast System and the TMI soil moisture data set. *J. Geophys. Res.*, 112. D03102, doi: 10.1029/2006JD007478.

Drusch, M., Holmes, T., de Rosnay, P., and Balsamo, G. (2009). Comparing ERA-40 based L-band brightness temperatures with Skylab observations: A calibration / validation study using the Community Microwave Emission Model. *J. Hydrometeo*. in press, doi: 10.1175/2008JHM964.1.

Dutra, E., Balsamo, G., Viterbo, P., Miranda, P., Beljaars, A., Schär, C., and Elder, K. (2010). An improved snow scheme for the ecmwf land surface model: description and offline validation. *J. Hydrometeo*, 11:899–916. doi: 10.1175/2010JHM1249.1.

Eagleman, J. and Lin, W. (1976). Remote sensing of soil moisture by a 21-cm passive radiometer. *J. Geophys. Res.*, 81:3660–3666.

Entekhabi, D., Njoku, E., O'Neill, P., Kellog, K., Crow, W., Edelstein, W., Entin, J., Goodman, S., Jackson, T., Johnson, J., Kimball, J., Piepmeier, J., Koster, R., Martin, N., McDonald, K., Moghaddam, M., Moran, S., Reichle, R., Shi, J., Spencer, M., Thurman, S., Tsang, L., and Van Zyl, J. (2010). The SoilMoistureActive Passive (SMAP) Mission. *Proceedings of the IEEE*, 98(5):704–716.

Escorihuela, M.-J., Kerr, Y. H., de Rosnay, P., Wigneron, J.-P., Calvet, J.-C., and Lemaître, F. (2007). A simple model of the bare soil microwave emission at l-band. *IEEE Trans. Geosc. Remote Sens.*, 45(7):1978–1987.

FAO (2003). FAO Digital Soil Map of the World (DSMW). In *Food and Agriculture Organization, Technical report of the United Nations*.

Holmes, T., de Rosnay, P., de Jeu, R., Wigneron, J.-P., Kerr, Y. H., Calvet, J.-C., Escorihuela, M.-J., Saleh, K., and Lemaître, F. (2006). A new parameterization of the Effective Temperature for L-band Radiometry. *Geophy. Res. Letters*, 33. L07405, doi:10.1029/2006GL025724.

Holmes, T., Drusch, M., Wigneron, J.-P., and de Jeu, R. (2008). A global simulation of microwave emission: Error structures based on output from ECMWFs operational Integrated Forecast System. *IEEE Trans. Geosc. Remote Sens.*, 46(3):846–856.

Jackson, T. and O'Neill, P. (1990). Attenuation of soil microwave emission by corn and soybeans at 1.4and 5 ghz. *IEEE Trans. Geosc. Remote Sens.*, 28(5):978–980.

Kerr, Y., Al-Yaari, A., Rodríguez-Fernández, N., Parrens, M., Molero, B., Leroux, D., Bircher, S., Mahmoodi, A., Mialon, A., Richaume, P., Delwart, S., Al Bitar, A., Pellarin, T., Bindlish, R., Jackson, T. J., Rüdiger, C., Waldteufel, P., Mecklenburg, S., and Wigneron, J.-P. (2016). Overview of SMOS performance in terms of global soil moisture monitoring after six years in operation. *Remote sens. environ.*, 180:40–63.

Kerr, Y. H., Waldteufel, P., Richaume, P., Wigneron, J.-P., Ferrazzoli, P., Mahmoodi, A., Al Bitar, A., Cabot, F., Gruhier, C., Juglea, S., Leroux, D., A., M., and Delwart, S. (2012). The SMOS soil moisture retrieval algorithm. *IEEE Transactions on Geoscience and Remote Sensing*, 50:1384–1403.

Kerr, Y. H., Waldteufel, P., Wigneron, J.-P., Cabot, F., Boutin, J., Escorihuela, M., Font, J., Reul, N., Gruhier, C., Juglea, S., Delwart, S., Drinkwater, M., Hahne, A., Martin-Neira, M., and Mecklenburg, S. (2010). The SMOS mission: new tool for monitoring key elements of the global water cycle. *Proceedings of the IEEE*, 98(5):666–687. doi:10.1109/JPROC.2010.2043032.

Kirdyashev, K., Chukhlantsev, A., and Shutko, A. (1979). Microwave radiation of the earths surface in the presence of vegetation cover. *Radiotekhnika i Elektronika*, 24:256–264.

Koster, R., Mahanama, P., Yamada, T., Balsamo, G., Berg, A., Boisserie, M., Dirmeyer, P., Doblas-Reyes, F., Drewitt, G., Gordon, C., Guo, Z., Jeong, J., Lee, W., Li, Z., Luo, L., Malyshev, S., Merryfield, W., Seneviratne, S., Stanelle, T., van den Hurk, B., Vitart, F., and Wood, E. (2011). The second phase of the global land-atmosphere coupling experiment: soil moisture contributions to subseasonal forecast skill. *J. Hydrometeo*, 12:805–822.

Koster, R. D., Dirmeyer, P., Guo, Z., Bonan, G., Cox, P., Gordon, C., Kanae, S., Kowalczyk, E., Lawrence, D., Liu, P., Lu, C., Malyshev, S., McAvaney, B., Mitchell, K., Mocko, D., Oki, T., Oleson, K., Pitman, A., Sud, Y., Taylor, C., Verseghy, D., Vasic, R., Xue, Y., and Yamada, T. (2004). Regions of strong coupling between soil moisture and precipitation. *Sciences*, 305:1138–1140.

Kumar, S., Peters-Lidard, C, D., Mocko, D., Reichle, R., Liu, Y., Arsenault, K. R., Xia, Y., Ek, M., Riggs, G., Livneh, B., and Cosh, M. (2014). Assimilation of remotely sensed soil moisture and snow depth retrievals fo drought estimation. *J. Hydrometeo*, 15:2446–2469.

Lievens, H., Al Bitar, A., Verhoest, N., Cabot, F., De Lannoy, G., Drusch, M., Dumedah, G., Hendricks Franssen, H., Kerr, Y., Tomer, S., Martens, B., Merlin, O., Pan, M., , van den Berg, M., Vereecken, H., Walker, J., Wood, E., and Pauwels, V. (2015). Optimization of a Radiative Transfer Forward Operator for Simulating SMOS Brightness Temperatures over the Upper Mississippi Basin. *J. Hydrometeo*, 16:1109–1134.

Loveland, T., Reed, B., Brown, J., D.O., O., Zhu, Z., Youing, L., and Merchant, J. (2000). Development of a global land cover characteristics

database and igb6cover from the 1km avhrr data. *Int. J. Remote Sens.*, 21:1303–1330.

Mecklenburg, S., Drusch, M., Kaleschke, L., Rodríguez-Fernández, N., Reul, N., Kerr, Y., Font, J., Martin-Neira, M., Oliva, R., Daganzo-Eusebio, E., Grant, J., Sabia, R., Macelloni, G., Rautiainen, K., Fauste, J., de Rosnay, P., Muñoz Sabater, J., Verhoest, N., Lievens, H., Delwart, S., Crapolicchio, R., de la Fuente, A., and Kornbe, M. (2016). ESA's Soil Moisture and Ocean Salinity mission: From science to operational applications. *Remote sens. environ.*, 180:3–18. doi:10.1016/j.rse.2015.12.025.

Mialon, A., Wigneron, J.-P., de Rosnay, P., Escorihuela, M., and Ker, Y. (2012). Evaluation the L-MEB model from long-term microwave measurements over a rough field, SMOSREX 2006. *IEEE Trans. Geosc. Remote Sens.*, 50(5):1458–1467.

Mironov, V., Dobson, M., Kaupp, V., Komarov, S., and Kleshchenko, V. (2004). Generalized refractive Mixing dielectric model for moist soils. *IEEE Trans. Geosc. Remote Sens.*, 42(4):773–785.

Muñoz Sabater, J., de Rosnay, P., Albergel, C., and Isaksen, L. (2018a). Sensitivity of soil moisture analyses to contrasting background and observation error scenarios. *Water*, 10(7).

Muñoz Sabater, J., de Rosnay, P., and Balsamo, G. (2011a). Sensitivity of L-band NWP forward modelling to soil roughness. *Int J. of Remote Sensing*. doi:10.1080/01431161.2010.507260.

Muñoz Sabater, J., de Rosnay, P., Jiménez, C., Isaksen, L., and Albergel, C. (2014). SMOS brightness temperatures angular noise: characterization, filtering and validation. *IEEE Transactions on Geoscience and Remote Sensing*, 52(9):5827–5839.

Muñoz Sabater, J., Fouilloux, A., and de Rosnay, P. (2011b). Technical implementation of SMOS data in the ECMWF Integrated Forecasting System. *IEEE Trans. Geosc. Remote Sens.* doi: 10.1109/LGRS.2011.2164777.

Muñoz Sabater, J., Lawrence, H., Albergel, C., de Rosnay, P., Isaksen, L., Drusch, M., Kerr, Y., and Mecklenburg, S. (2018b). Assimilation of SMOS brightness temperature in the ECMWF Integrated Forecasting System. in preparation for QJRMS.

Muñoz Sabater, J., Rodríguez-Fernández, N., Richaume, P., de Rosnay, P., and Kerr, Y. (2016). SMOS Near-real-Time Soil Moisture: product description . *ESA contract 4000101703/10/NL/FF/fk, WP4020.*

Njoku, E. G., Jackson, T., Lakshmi, V., Chan, T., and Nghiem, S. (2003). Soil moisture retrieval from AMSR-E. *IEEE Trans. Geosc. Remote Sens.*, 41(2):215–229.

Pellarin, T., Wigneron, J.-P., Calvet, J.-C., Berger, M., Douville, H., Ferrazzoli, P., Kerr, Y. H., Lopez-Baeza, E., Pulliainen, J., Simmonds, L., and Waldteufel, P. (2003). Two-year global simulation of L-band brightness temperature over land. *IEEE Trans. Geosc. Remote Sens.*, 41(4):2135–2139.

Pulliainen, J., Hallikainen, M., and Grandell, J. (1999). HUT snow emission model and its applicability to snow water equivalent retrieval. *IEEE Trans. Geos. Remot. Sens*, 37:1378–1390.

Reichle, R. H., De Lannoy, G., Forman, B., Liu, Q., Mahanama, S., and Toure, A. (2011). Assessment and enhancement of MERRA land surface hydrology estimates. *J. Climate.*, 24:6322–6338.

Reichle, R. H. and Koster, R. D. (2004). Bias reduction in short reccords of satellite soil moisture. *Geophy. Res. Letters*, 31.

Richards, L. A. (1931). *Capillary conduction of liquids in porous medium*. Physics 1.

Rodriguez, N., Muñoz Sabater, J., Richaume, P., de Rosnay, P., Kerr, Y., Albergel, C., Drusch, M., and Mecklenburg, S. (2017). SMOS near-real-time soil moisture product: processor overview and first validation results. *Hydrology and Earth System Sciences*, 21:5201–5216.

Rodriguez, N., Richaume, P., Muñoz Sbater, J., de Rosnay, P., and Kerr, Y. (2016). SMOS Near-real-Time Soil Moisture processor: recommended neural network configuration and algorithm description. *ESA contract 4000101703/10/NL/FF/fk, WP4020 SO-TN-CB-GS-0049*.

Scipal, K., Drusch, M., and Wagner, W. (2008). Assimilation of a ers scatterometer derived soil moisture index in the ecmwf numerical weather prediction system. *Advances in Water Resources*. doi: 10.1016/j.advwatres.2008.04.013.

Taylor, C. and Clark, D. (2001). The diurnal cycle and African easterly waves: A land surface perspective. *Quart. J. Roy. Meteorol. Soc.*, 127:845–867.

Taylor, C., de Jeu, R., Guichard, F., P., H., and Dorigo, W. (2012). Afternoon rain more likely over dry soils. *Nature*, 489:423–426. 10.1038/nature11377.

Trenberth, K., Smith, L., Qian, T., Dai, A., and Fasullo, J. (2007). Estimates of the global water budget and its annual cycle using observational

and model data. *J. Hydrometeo*, 8:758–769.

Ulaby, F., Moore, R., and Fung, A. (1986). In *Microwave remote sensing: active and passive, Vol III, from theory to application*. Artech House, Dedham, MA.

Viterbo, P. and Beljaars, A. C. M. (1995). An improved land surface parameterization scheme in the ECMWF model and its validation. Technical report, 75, ECMWF.

Wagner, W., Hahn, S., Kidd, R., Melzer, T., Bartalis, Z., Hasenauer, S., Figa-Saldaña, J., de Rosnay, P., Jann, A., Scheiner, S., Komma, J., Kubu, G., Brugger, K., Aubrecht, C., Züger, J., Gangkofner, U., Kienberger, S., Brocca, L., Wang, Y., Blöschl, G., Eitzinger, J., Steinnocher, K., Zeil, P., and Rubel, F. (2013). The ascat soil moisture product: A review of its specifications, validation results, and emerging applications. *Meteorologische Zeitschrift*, 22(1):5–33. doi: 10.1127/0941-2948/2013/0399.

Wanders, N., Karssenberg, D., de Roo, A., de Jong, S., and Bierkens, M. (2014). The suitability of remotely sensed soil moisture for improving operational flood forecasting. *Hydrology and Earth System Sciences*, 18:2343–2357. doi:10.5194/hess-18-2343-2014.

Wang, J. R. and Choudhury, B. (1981). Remote sensing of soil moisture content over bare field at 1.4 ghz frequency. *J. Geophys. Res.*, 86:5277–5282.

Wang, J. R. and Schmugge, T. (1980). An empirical model for the complex dielectric permittivity of soils as a function of water content. *IEEE Trans. Geosc. Remote Sens.*, 18:288–295.

Wegmüller, U. and Mätzler, C. (1999). Rough bare soil reflectivity model. *IEEE Transactions on Geoscience Electronics*, 37:1391–1395.

Wegmüller, U., Mätzler, C., and Njoku, E. (1995). Canopy opacity models, in passive microwave remote sensing of land-atmosphere interactions. *B. et al. Ed. Utrecht, The Netherlands: VSP*, page 375.

Wigneron, J.-P., Kerr, Y. H., Waldteufel, P., Saleh, K., Escorihuela, M.-J., Richaume, P., Ferrazzoli, P., de Rosnay, P., Gurney, R., Calvet, J.-C., Guglielmetti, M., Hornbuckle, B., Mätzler, C., Pellarin, T., and Schwank, M. (2007). L-band Microwave Emission of the Biosphere (L-MEB) Model: description and calibration against experimental data sets over crop fields. *Remote sens. environ.*, 107:639–655.

Wigneron, J.-P., Laguerre, L., and Kerr, Y. H. (2001). A Simple Parmeterization of the L-band Microwave Emission from Rough Agricultural Soils. *IEEE Trans. Geosc. Remote Sens.*, 39:1697–1707.

Yilmaz, T. and Crow, W. (2013). The optimality of potential rescaling approaches in land data assimilation. *J. Hydrometeo*, 14:650–660.

List of Figures

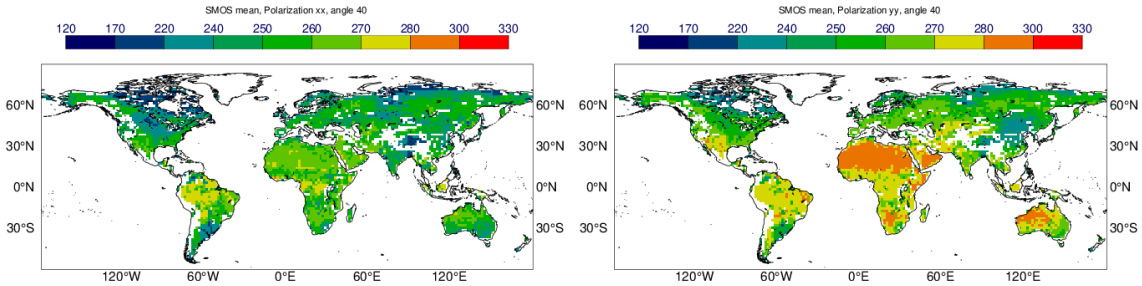

(a) SMOS Observations (K)

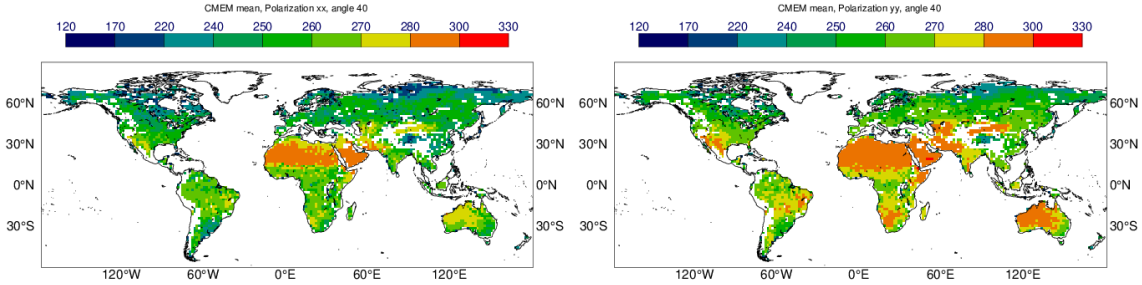

(b) ECMWF_CMEM Model simulations (K)

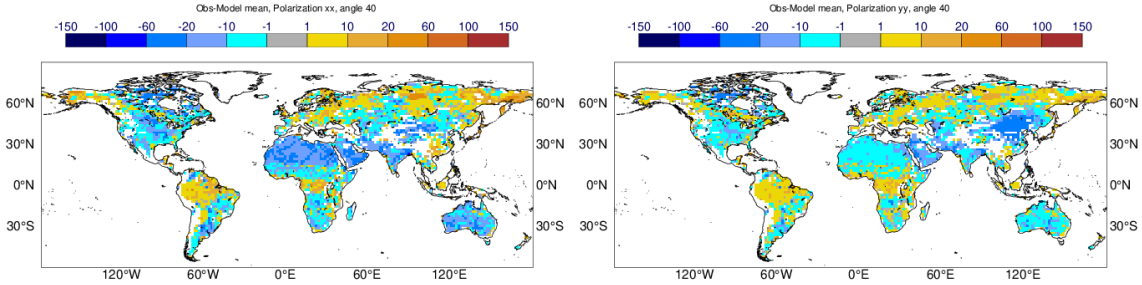

(c) First Guess Departure (Observation - Model) (K)

Figure 1: L-band brightness temperature (K) annual mean maps (2010-2011), at 40° incidence angle, xx polarisation (left) and yy polarisation (right), observed by SMOS (a), simulated by ECMWF (b), and first guess departure (Observation-Model, c). ECMWF brightness temperatures shown here are obtained from one of the Set1 experiments (Table 2), using the dielectric model of Wang and Schmugge (1981), the simple soil roughness Model of Wigneron et al. (2001) and the Wigneron et al. (2007) vegetation opacity model.

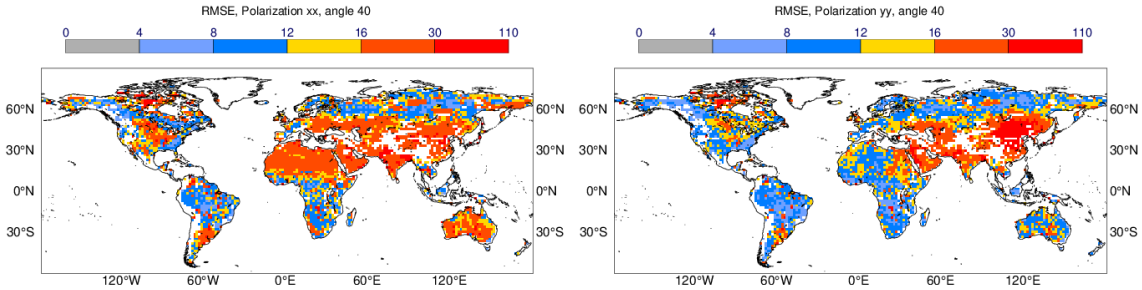

(a) RMSE (K)

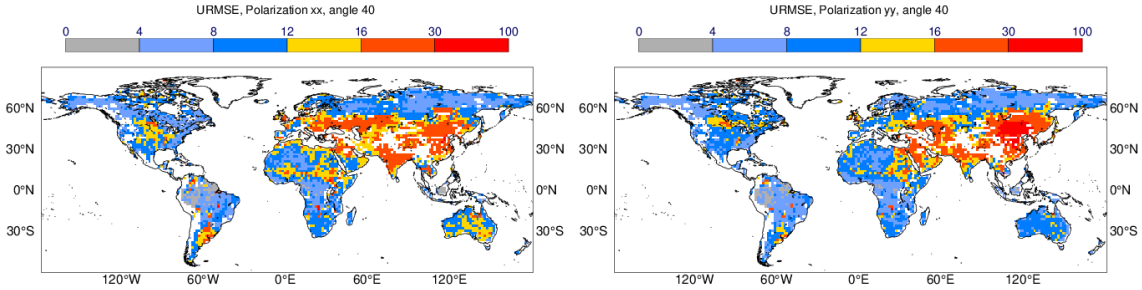

(b) URMSE (K)

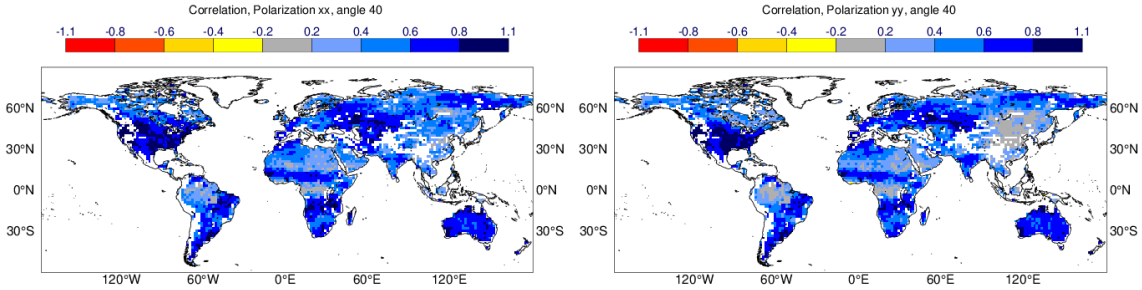

(c) Correlation

Figure 2: Comparison between SMOS observations and simulated L-band brightness temperature for 2010-2011, at 40° incidence angle, at xx polarisation (left) and yy polarisation (right): RMSE (a), URMSE (b) and correlation (c). ECMWF brightness temperatures shown here are obtained from one of the Set1 experiments (Table 2), using the dielectric model of Wang and Schmugge, the simple soil roughness Model of Wigneron et al., 2001 and the Wigneron et al., 2007 vegetation opacity model.

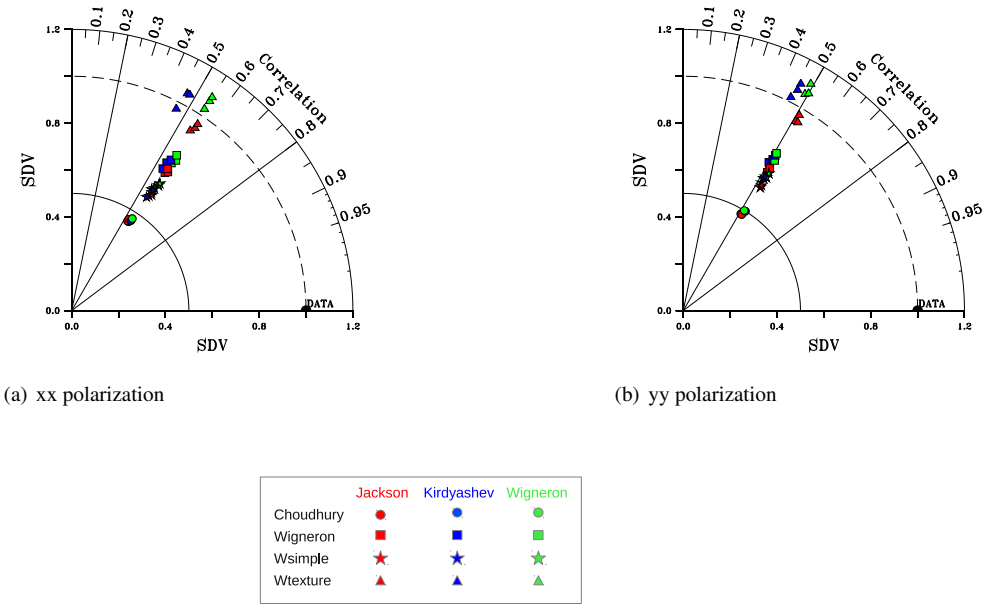

(a) xx polarization

(b) yy polarization

Figure 3: Comparison between ECMWF simulated and SMOS measured brightness temperatures at L-band (1.4 GHz) at xx (left) and yy (right) polarisations, for 2010-2011 for 36 CMEM configurations of Set 1 experiments (see Tables 1 and 2). Symbols colour and shapes represent different vegetation opacity and roughness models, respectively; and for each three identical symbols are used for the different dielectric models.

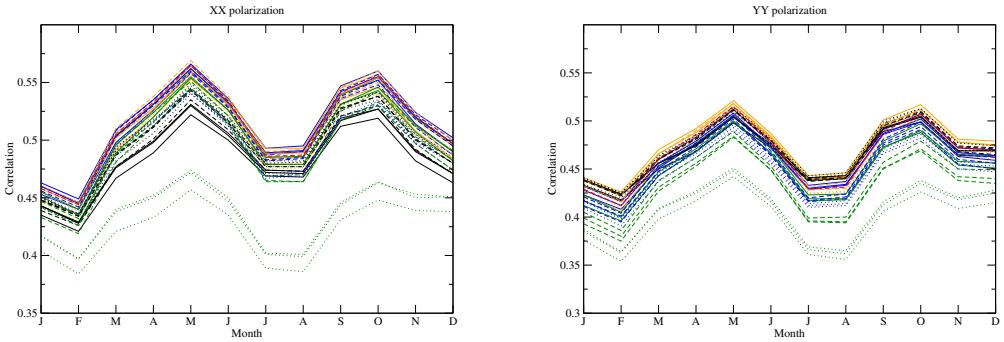

(a) Correlation

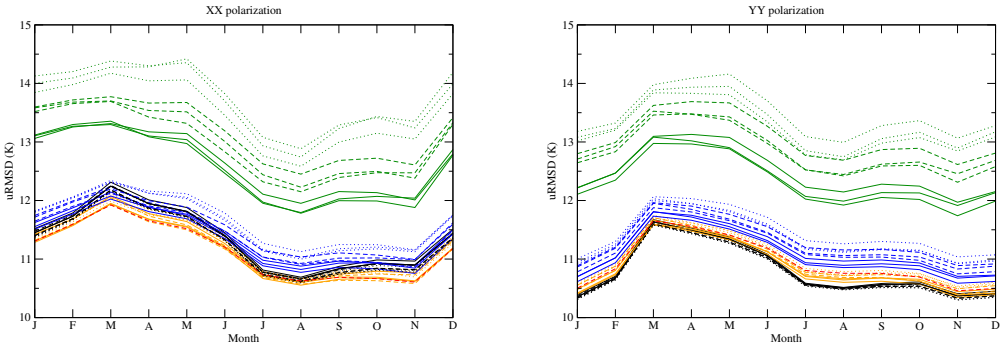

(b) Unbiased RMSE

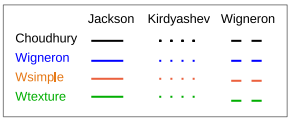

Figure 4: Annual cycle of the global mean correlation (top) and URMSD (bottom) between L-band brightness temperatures observations from SMOS and ECMWF forward simulations for the 36 CMEM configurations of Set 1 experiments (see Tables 1 and 2), at xx (left) and yy (right) polarisations, for a 40° incidence angle. Statistics are computed on the period 2010-2011.

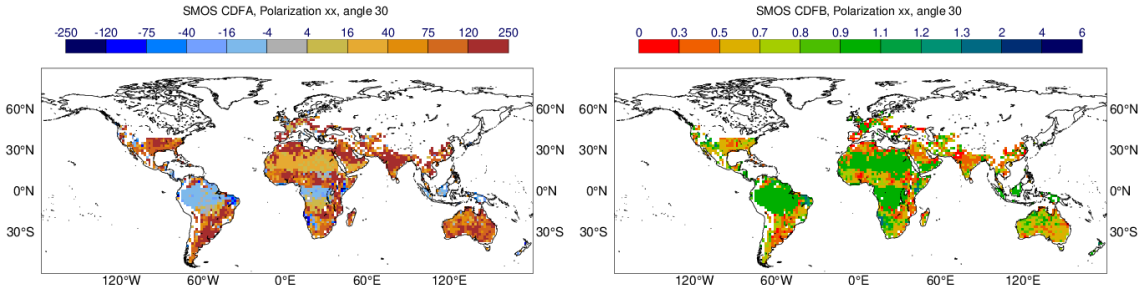

(a) Angle 30°

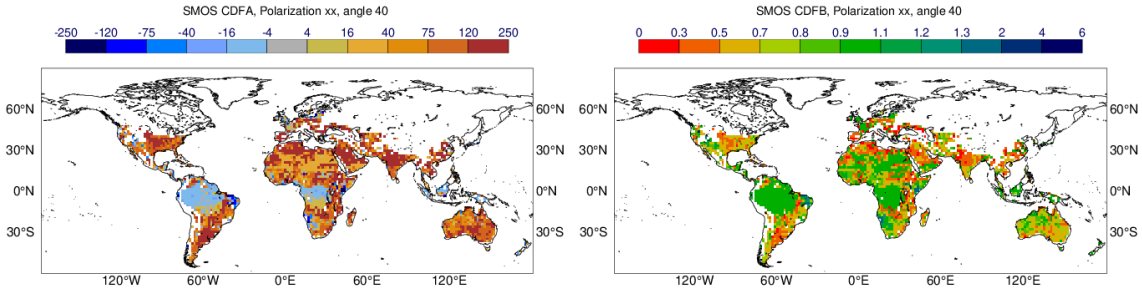

(b) Angle 40°

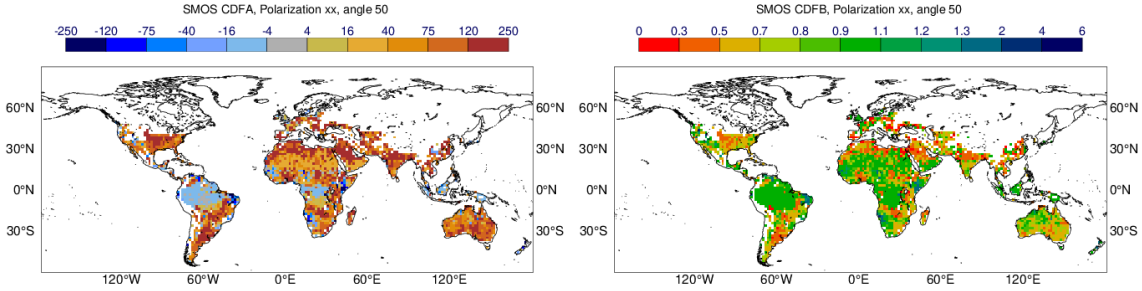

(c) Angle 50°

Figure 5: ECMWF monthly CDF matching parameters A (left) and B (right), for January, at xx polarization, computed at 40km resolution, at 30^{circ} (top panel), 40^{circ} (middle panel) and 50^{circ} (bottom panel), for the default CMEM configuration using the dielectric model of Wang and Schmugge, the simple soil roughness Model of Wigneron et al., 2001 and the Wigneron et al., 2007 vegetation opacity model.

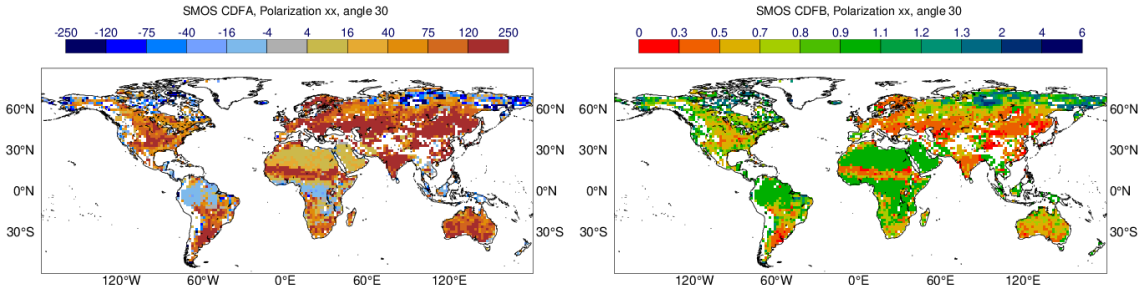

(a) Angle 30°

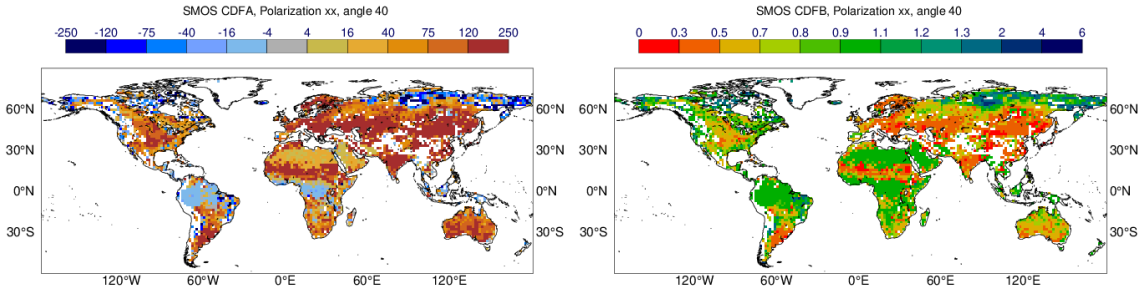

(b) Angle 40°

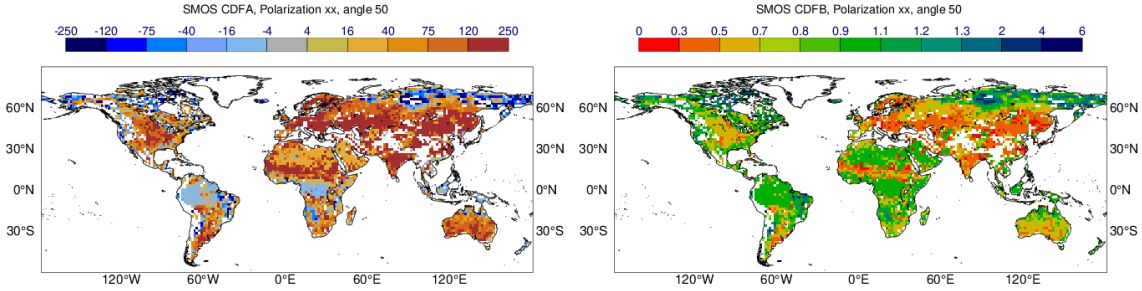

(c) Angle 50°

Figure 6: ECMWF monthly CDF matching parameters A (left) and B (right), for July in xx polarization, computed at 40km resolution, at 30^{circ} (top panel), 40^{circ} (middle panel) and 50^{circ} (bottom panel), for the default CMEM configuration using the dielectric model of Wang and Schmugge, the simple soil roughness Model of Wigneron et al., 2001 and the Wigneron et al., 2007 vegetation opacity model.

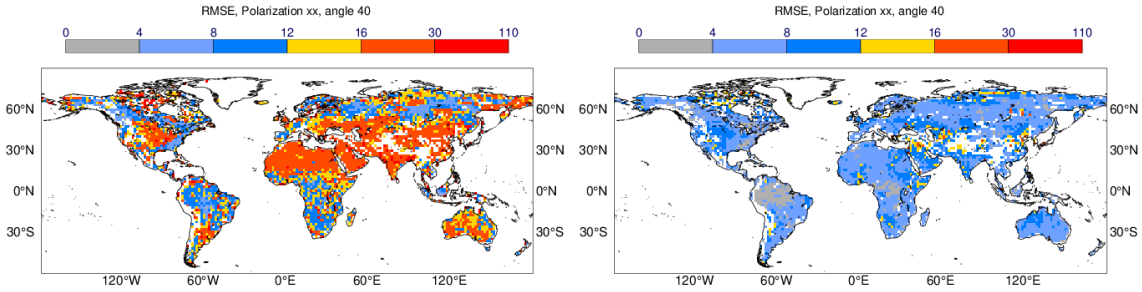

(a) RMSE (K)

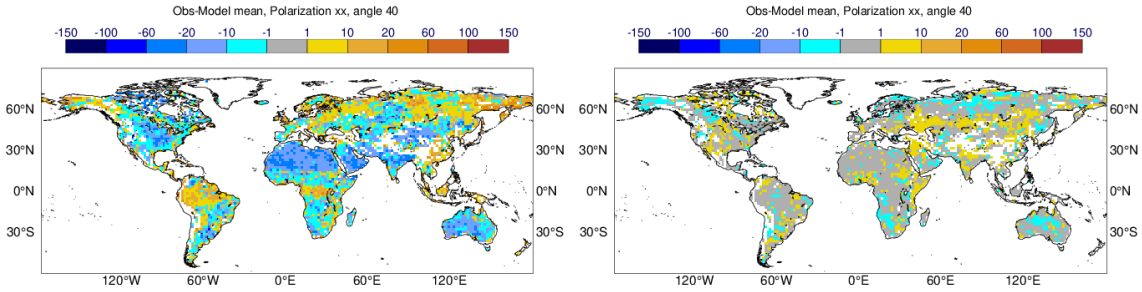

(b) Bias (Observation - Model) (K)

Figure 7: Comparison between ECMWF CMEM and SMOS brightness temperatures before (left) and after (right) bias correction for 2013 xx pol and 40° incidence angle. Panels a and b show RMSE (K) and bias (K), respectively.

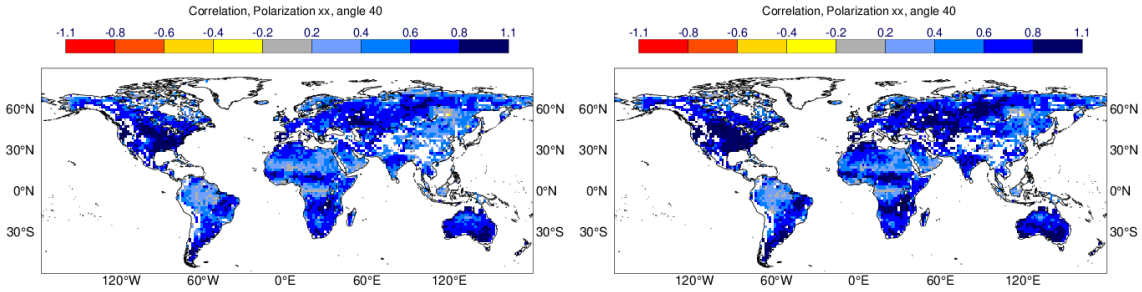

(a) Correlation

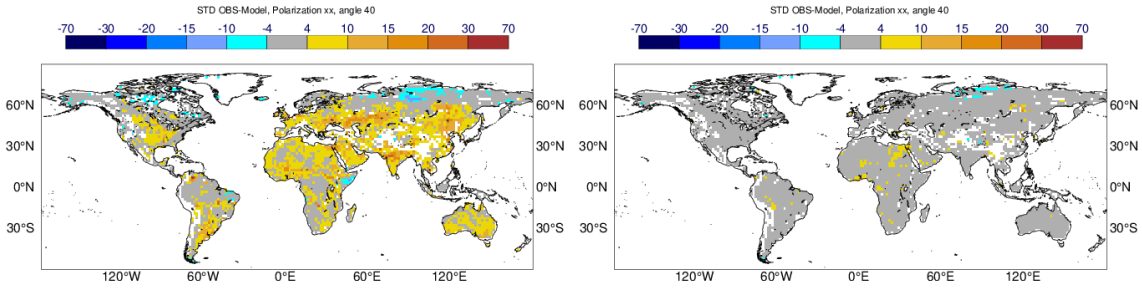

(b) STD difference (Observation - Model) (K)

Figure 8: Comparison between ECMWF CMEM and SMOS brightness temperatures before (left) and after (right) bias correction for 2013 xx pol and 40° incidence angle. Panels a and b show correlation and STD (K) difference, respectively.

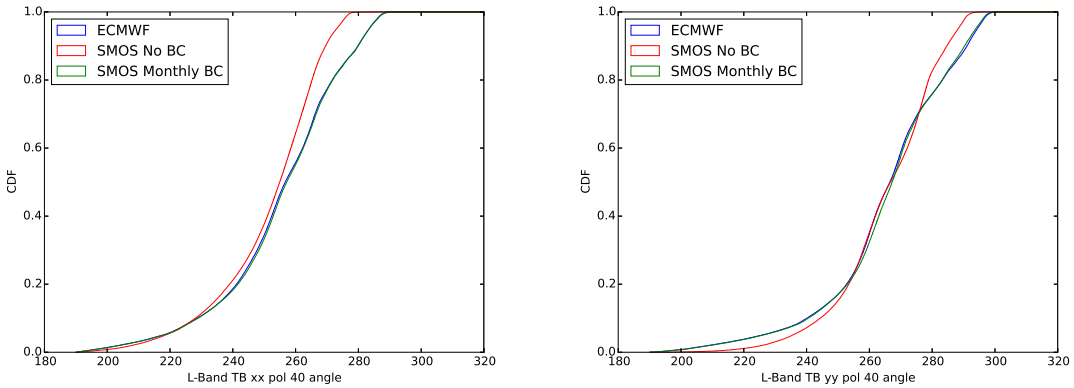

(a) xx pol

(b) yy pol

Figure 9: Cumulative Distribution Function of SMOS observed brightness temperatures (red), ECMWF reanalysed brightness temperatures (blue) and monthly CDF-matched SMOS brightness temperatures (green) for 2013 at xx pol (left) and yy pol (right) at 40° incidence angle for 2010-2014.

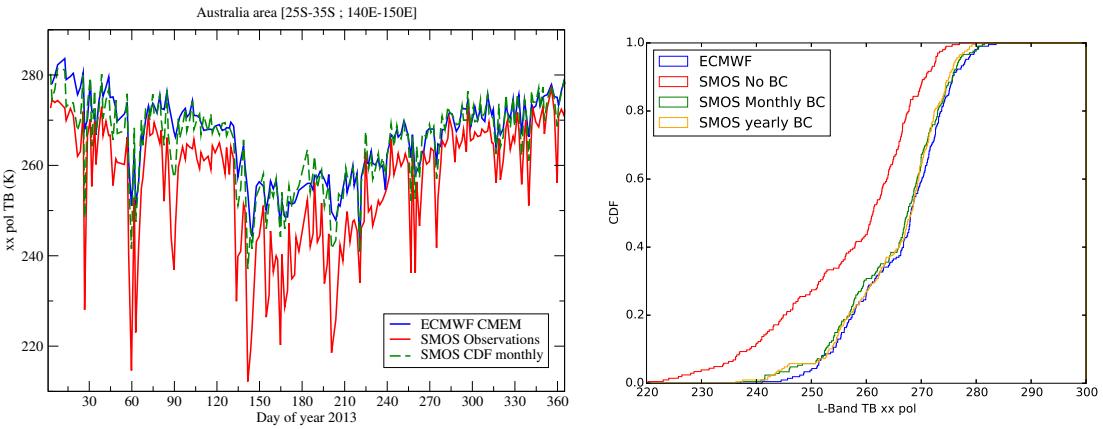

(a) Australia

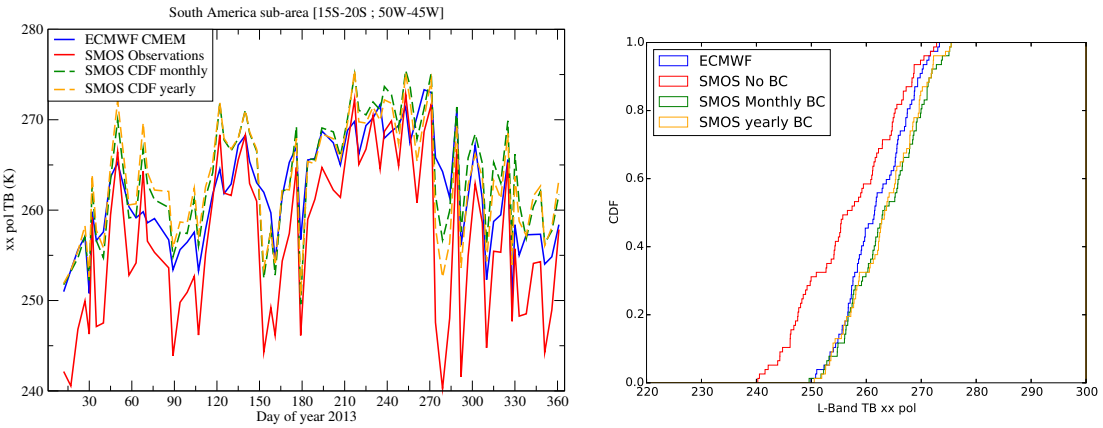

(b) South America

Figure 10: Annual cycle (left) and CDF (right) for 2013 of xx pol brightness temperature (in K), at 40° incidence angle, simulated by ECMWF CMEM (blue), observed by SMOS (red) and matched using monthly CDF matching (green), for two areas located in Australia (a) and South America (b).

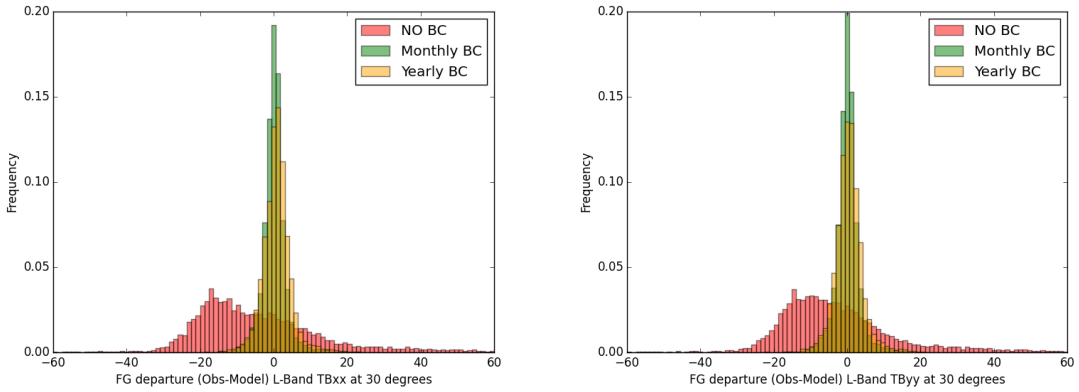

(a) Angle 30°

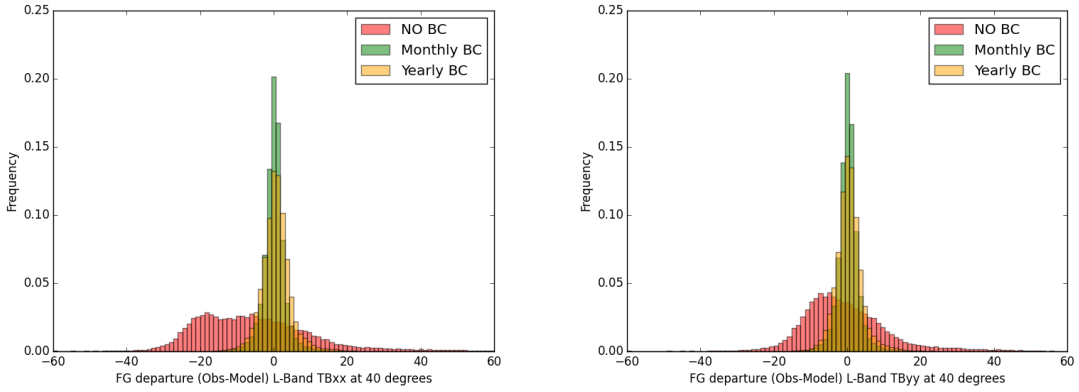

(b) Angle 40°

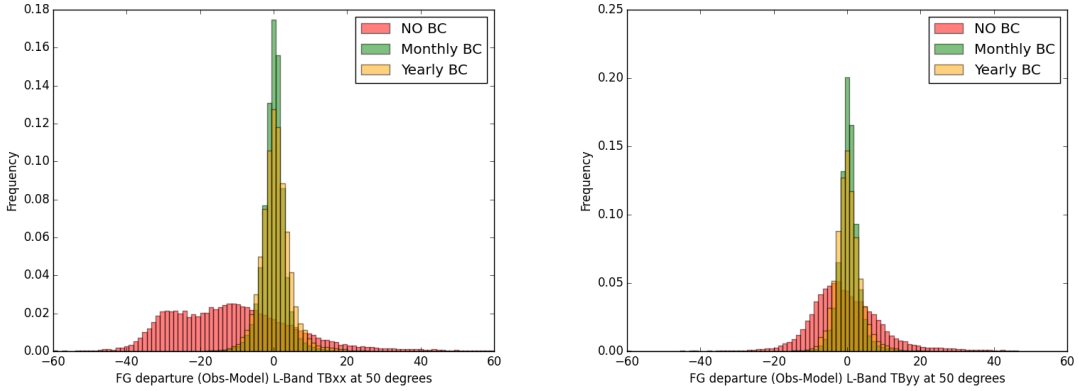

(c) Angle 50°

Figure 11: Histograms of monthly mean first guess departures (Observation - Model in K) for January 2013 for xx pol (left) and yy pol (right), for incidence angles of 30° (a), 40° (b), 50° (c). Red, green and orange colours show first guess departure distribution with no bias correction (red), monthly bias correction (green) and yearly bias correction (yellow), respectively.

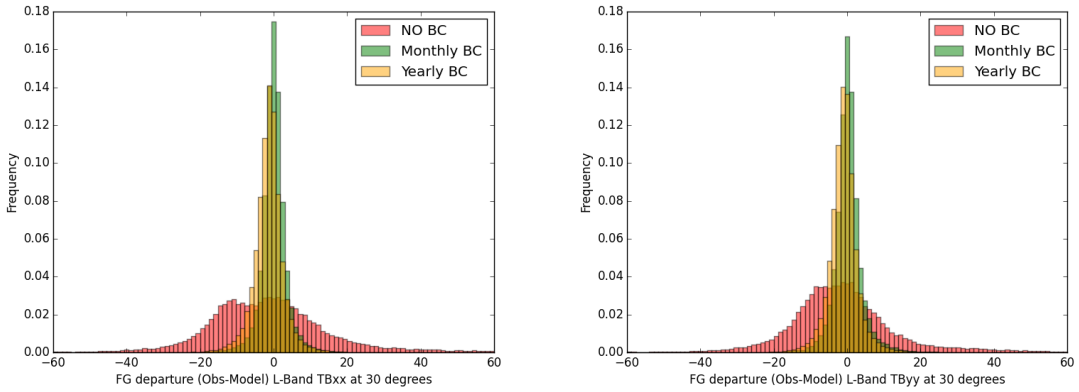

(a) Angle 30°

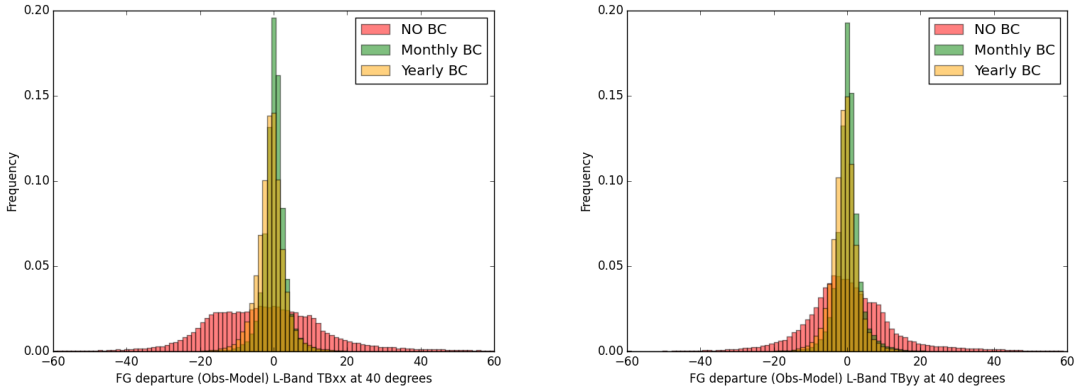

(b) Angle 40°

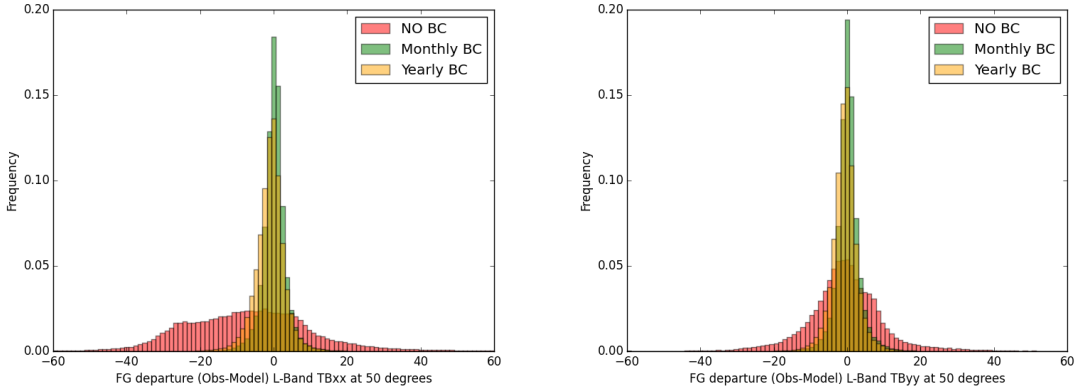

(c) Angle 50°

Figure 12: Histograms of monthly mean first guess departures (Observation - Model in K) for July 2013 for xx pol (left) and yy pol (right), for incidence angles of 30° (a), 40° (b), 50° (c). Red, green and orange colours show first guess departure distribution with no bias correction (red), monthly bias correction (green) and yearly bias correction (yellow), respectively.

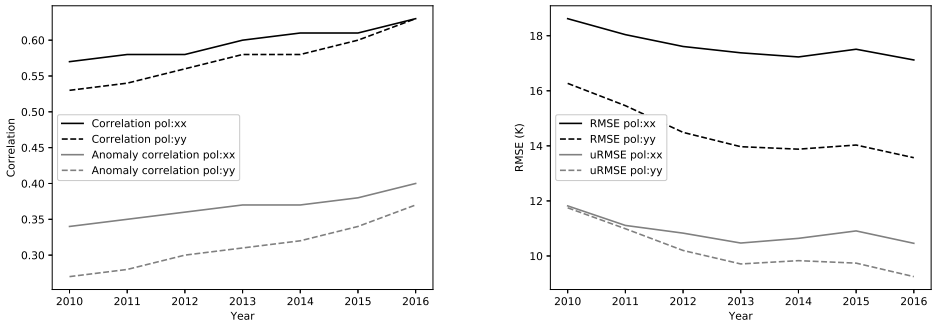

(a) Correlation

(b) Root mean square error

Figure 13: Global mean statistics of SMOS brightness temperatures monitoring from 2010 to 2016, comparing SMOS observations to ECMWF CMEM reanalysis of L-Band brightness temperature, at 40° incidence angle, at xx (solid line) and yy (dashed line) polarisations. Left panel show correlation (black) and anomaly correlation (grey). Right panel shows RMSE (black) and uRMSE (grey).

List of Tables

CMEM modules	Choice of parameterizations	
	Short name	Reference
Soil module:		
Dielectric mixing model	**Dobson**	(Dobson et al., 1985),
	Mironov	(Mironov et al., 2004)
	Wang	(Wang and Schmugge, 1980)
Effective temperature model	Surface temperature forcing,	
	Choudhury	(Choudhury et al., 1982)
	Wigneron	(Wigneron et al., 2001)
	Holmes	(Holmes et al., 2006)
Soil roughness model	**Choudhury**	(Choudhury et al., 1979),
	Wigneron	(Wigneron et al., 2007)
	Wsimple	(Wigneron et al., 2001)
	Wtexture	(ATBD, 2007)
	Wegmüller	(Wegmüller and Mätzler, 1999)
Vegetation module:		
Vegetation optical depth model	Wegmüller	(Wegmüller et al., 1995),
	Jackson	(Jackson and O'Neill, 1990)
	Kirdyashev	(Kirdyashev et al., 1979)
	Wigneron	(Wigneron et al., 2007)
Snow module:		
Snow emission model	HUT single layer model	(Pulliainen et al., 1999)
Atmospheric module:		
Atmospheric emission model	**Pellarin**	(Pellarin et al., 2003),
	Ulaby	(Ulaby et al., 1986)

Table 1: Modular configuration of CMEM. For each module components, a choice of parameterizations is available. Parameterizations in bold are those used in this paper. Different combinations of CMEM using three different dielectric models, four roughness models and three vegetation optical depths models are compared, leading to 36 configurations evaluated against SMOS observations.

Objective	Set name	Number of runs	Period	Resolution	Incidence angle	SMOS processor	Results
CMEM configuration	Set 1	36	2010-2011	80 km (TL255)	40°	v5	Section 3.1
Bias correction	Set 2	1	2010-2013	40km (TL511)	30° , 40° , 50°	v5	Section 2.5
Long term monitoring	Set 3	1	2010-2016	40km (TL511)	40°	v5 (until 04.2015) v6 (from 05.2015)	Section 3.3

Table 2: Description of the numerical experiments conducted to address the three objectives of the paper: for model configuration, bias correction and long term monitoring. The 36 experiments of Set 1 use different CMEM configurations corresponding to different combinations of parameterisations shown in Table 1. Experiments conducted for Set 2 and Set 3 rely on the best CMEM configuration selected after Set 1 experiments are compared to SMOS data.

Dielectric Model	Vegetation Opacity Model	Soil Roughness Model	R	uRMSE (K)	Bias (K)	SDV
Dobson	Jackson	Choudhury	0.53	12.00	-20.92	0.45
		Wigneron	**0.56**	11.90	**-0.16**	0.71
		Wsimple	**0.56**	11.77	-7.13	0.59
		Wtexture	0.55	13.20	17.17	0.92
	Kirdyashev	Choudhury	0.54	11.90	-20.04	0.45
		Wigneron	0.54	12.14	5.71	0.72
		Wsimple	0.55	11.82	-2.30	0.58
		Wtexture	0.46	14.28	29.10	**0.97**
	Wigneron	Choudhury	0.54	11.92	-19.06	0.46
		Wigneron	**0.56**	11.96	5.09	0.76
		Wsimple	**0.56**	**11.70**	-2.20	0.63
		Wtexture	0.55	13.57	27.65	**1.03**
Mironov	Jackson	Choudhury	0.53	11.93	-21.98	0.45
		Wigneron	**0.57**	11.81	-3.15	0.72
		Wsimple	**0.57**	11.65	-9.69	0.60
		Wtexture	0.56	13.21	12.01	0.94
	Kirdyashev	Choudhury	0.55	11.82	-21.29	0.46
		Wigneron	0.54	12.17	2.18	0.75
		Wsimple	0.55	11.76	-5.34	0.62
		Wtexture	0.48	14.61	22.96	**1.05**
	Wigneron	Choudhury	0.55	11.84	-20.24	0.47
		Wigneron	**0.57**	11.91	**1.76**	0.78
		Wsimple	**0.57**	**11.60**	-5.08	0.65
		Wtexture	0.55	13.72	21.86	1.07
Wang	Jackson	Choudhury	0.53	11.94	-21.60	0.46
		Wigneron	0.56	11.90	-1.96	0.73
		Wsimple	0.56	11.67	-8.78	0.61
		Wtexture	0.56	13.32	13.84	**0.96**
	Kirdyashev	Choudhury	0.55	11.81	-20.92	0.46
		Wigneron	0.55	12.23	3.33	0.77
		Wsimple	0.56	11.74	-4.46	0.62
		Wtexture	0.48	14.63	24.74	1.05
	Wigneron	Choudhury	0.55	11.84	-19.86	0.47
		Wigneron	0.56	12.03	**2.95**	0.80
		Wsimple	**0.57**	**11.63**	-4.16	0.66
		Wtexture	0.55	13.90	23.70	1.09

Table 3: Statistics of the global scale comparison between ECMWF ERA-Interim-based CMEM simulations and SMOS observations of L-band brightness temperature at xx polarization for a 40° incidence angle for 2010-2011 for 36 CMEM configurations of Set 1 experiments (see Tables 1 and 2). For each dielectric model best statistics are highlighted in bold. SDV is the normalised standard deviation (ratio between the simulated and observed brightness temperature standard deviations).

Dielectric Model	Vegetation Opacity Model	Soil Roughness Model	R	uRMSE (K)	Bias (K)	SDV
Dobson	Jackson	Choudhury	0.51	11.46	-12.11	0.48
		Wigneron	0.52	11.66	-0.59	0.69
		Wsimple	**0.53**	11.47	-3.57	0.62
		Wtexture	0.51	13.07	11.16	0.94
	Kirdyashev	Choudhury	0.52	**11.38**	-12.12	0.49
		Wigneron	0.50	11.91	2.62	0.73
		Wsimple	0.52	11.54	-0.93	0.64
		Wtexture	0.45	14.01	18.57	**1.02**
	Wigneron	Choudhury	0.52	11.41	-11.01	0.49
		Wigneron	0.51	11.79	2.37	0.75
		Wsimple	0.52	11.49	**-0.51**	0.66
		Wtexture	0.49	13.57	17.81	1.06
Mironov	Jackson	Choudhury	0.52	11.42	-12.92	0.48
		Wigneron	0.52	11.60	-2.69	0.69
		Wsimple	**0.53**	11.39	-5.55	0.62
		Wtexture	0.52	13.02	7.24	**0.94**
	Kirdyashev	Choudhury	**0.53**	**11.34**	-13.10	0.50
		Wigneron	0.51	11.93	**0.04**	0.75
		Wsimple	0.52	11.52	-3.32	0.66
		Wtexture	0.46	14.16	13.78	**1.06**
	Wigneron	Choudhury	0.52	11.37	-11.93	0.49
		Wigneron	0.52	11.75	-0.00	0.75
		Wsimple	**0.53**	11.43	-2.75	0.67
		Wtexture	0.50	13.60	13.35	1.07
Wang	Jackson	Choudhury	0.52	11.42	-12.71	0.48
		Wigneron	0.52	11.71	-2.10	0.71
		Wsimple	**0.53**	11.44	-5.06	0.63
		Wtexture	0.51	13.23	8.21	0.97
	Kirdyashev	Choudhury	**0.53**	**11.34**	-12.91	0.50
		Wigneron	0.51	12.05	0.61	0.77
		Wsimple	0.52	11.56	-2.85	0.67
		Wtexture	0.46	14.38	14.72	**1.09**
	Wigneron	Choudhury	0.52	11.37	-11.73	0.50
		Wigneron	0.51	11.88	**0.60**	0.78
		Wsimple	**0.53**	11.49	-2.25	0.69
		Wtexture	0.49	13.87	14.34	1.11

Table 4: Statistics of the global scale comparison between ECMWF CMEM simulations and SMOS observations of L-band brightness temperature at yy polarization for a 40° incidence angle for 2010-2011 for 36 CMEM configurations if Set 1 experiments (see Tables 1 and 2). For each dielectric model best statistics are highlighted in bold. SDV is the normalised standard deviation (ratio between the simulated and observed brightness temperature standard deviations)

Angle	Year	pol	N	R	Confidence		Anomaly R	RMSE (K)	Bias (K)
30	2010	xx	101.63	0.57	0.43	0.69	0.32	18.06	-1.95
30	2011	xx	106.86	0.59	0.45	0.70	0.32	17.53	-1.10
30	2012	xx	94.66	0.59	0.44	0.71	0.33	17.11	-0.64
30	2013	xx	101.44	0.60	0.46	0.72	0.34	16.96	-1.01
40	2010	xx	150.17	0.57	0.45	0.67	0.34	18.62	-2.84
40	2011	xx	157.68	0.58	0.46	0.68	0.35	18.04	-1.91
40	2012	xx	139.84	0.58	0.46	0.68	0.36	17.61	-1.33
40	2013	xx	149.58	0.60	0.48	0.69	0.37	17.38	-1.64
50	2010	xx	148.28	0.51	0.37	0.62	0.27	20.64	-7.16
50	2011	xx	155.76	0.51	0.38	0.62	0.27	20.02	-6.48
50	2012	xx	138.50	0.52	0.38	0.63	0.27	19.57	-5.89
50	2013	xx	147.69	0.53	0.41	0.64	0.28	19.33	-6.26
30	2010	yy	101.00	0.58	0.43	0.69	0.33	17.30	-2.74
30	2011	yy	106.34	0.60	0.46	0.71	0.36	16.30	-1.73
30	2012	yy	94.44	0.62	0.47	0.73	0.39	15.34	-0.97
30	2013	yy	101.11	0.64	0.50	0.74	0.40	14.81	-0.97
40	2010	yy	146.74	0.53	0.40	0.64	0.27	16.27	-1.29
40	2011	yy	154.41	0.54	0.42	0.65	0.28	15.46	-0.24
40	2012	yy	136.88	0.56	0.43	0.66	0.30	14.49	0.43
40	2013	yy	146.83	0.58	0.46	0.68	0.31	13.97	0.55
50	2010	yy	140.68	0.49	0.35	0.61	0.24	15.14	-2.49
50	2011	yy	147.65	0.50	0.37	0.61	0.24	14.26	-1.37
50	2012	yy	130.59	0.53	0.39	0.64	0.27	13.29	-0.76
50	2013	yy	140.27	0.54	0.41	0.65	0.28	12.77	-0.55

Table 5: Statistics of the global scale comparison, before bias correction, between the ECMWF CMEM Set 2 experiment, using Wang and Schmugge, Wsimple and Wigneron parameterisations (see Tables 1 and 2), and SMOS observations of L-band brightness temperature at xx and yy polarizations for 30°, 40°, 50° incidence angles, for 2010-2013.

Angle	Year	pol	N	R	Confidence		Anomaly R	RMSE (K)	Bias (K)
30	2010	xx	102.08	0.64	0.50	0.74	0.31	7.95	-0.36
30	2011	xx	107.54	0.65	0.52	0.75	0.32	7.46	0.20
30	2012	xx	95.69	0.65	0.51	0.75	0.32	7.42	0.50
30	2013	xx	101.74	0.67	0.54	0.76	0.34	7.09	0.24
40	2010	xx	151.29	0.63	0.52	0.72	0.34	8.04	-0.42
40	2011	xx	159.04	0.64	0.54	0.73	0.35	7.53	0.18
40	2012	xx	141.95	0.65	0.54	0.73	0.35	7.48	0.55
40	2013	xx	150.50	0.67	0.56	0.75	0.37	7.13	0.35
50	2010	xx	148.95	0.57	0.44	0.67	0.26	8.96	-0.33
50	2011	xx	156.65	0.58	0.46	0.67	0.26	8.50	0.12
50	2012	xx	139.98	0.58	0.46	0.68	0.27	8.41	0.50
50	2013	xx	148.16	0.60	0.48	0.70	0.28	8.05	0.33
30	2010	yy	100.90	0.63	0.50	0.74	0.33	8.53	-0.76
30	2011	yy	106.17	0.66	0.53	0.76	0.35	7.64	-0.13
30	2012	yy	94.79	0.68	0.55	0.77	0.39	7.14	0.37
30	2013	yy	100.76	0.70	0.58	0.79	0.40	6.76	0.32
40	2010	yy	147.16	0.58	0.46	0.68	0.27	8.90	-0.84
40	2011	yy	154.34	0.60	0.49	0.69	0.28	8.16	-0.15
40	2012	yy	137.43	0.62	0.50	0.71	0.30	7.68	0.28
40	2013	yy	146.12	0.64	0.53	0.73	0.31	7.26	0.32
50	2010	yy	139.51	0.54	0.41	0.65	0.25	9.43	-1.17
50	2011	yy	145.79	0.56	0.43	0.66	0.25	8.66	-0.36
50	2012	yy	129.31	0.58	0.45	0.69	0.28	8.07	0.14
50	2013	yy	137.93	0.60	0.47	0.70	0.29	7.75	0.16

Table 6: Statistics of the global scale comparison, after bias correction, between the ECMWF CMEM Set 2 experiment, using Wang and Schmugge, Wsimple and Wigneron parameterisations (see Tables 1 and 2), and SMOS observations of L-band brightness temperature at xx and yy polarizations for 30°, 40°, 50° incidence angles, for 2010-2013.